Cell Reports

Article

Kmt2c mutations enhance HSC self-renewal capacity and convey a selective advantage after chemotherapy

Graphical Abstract

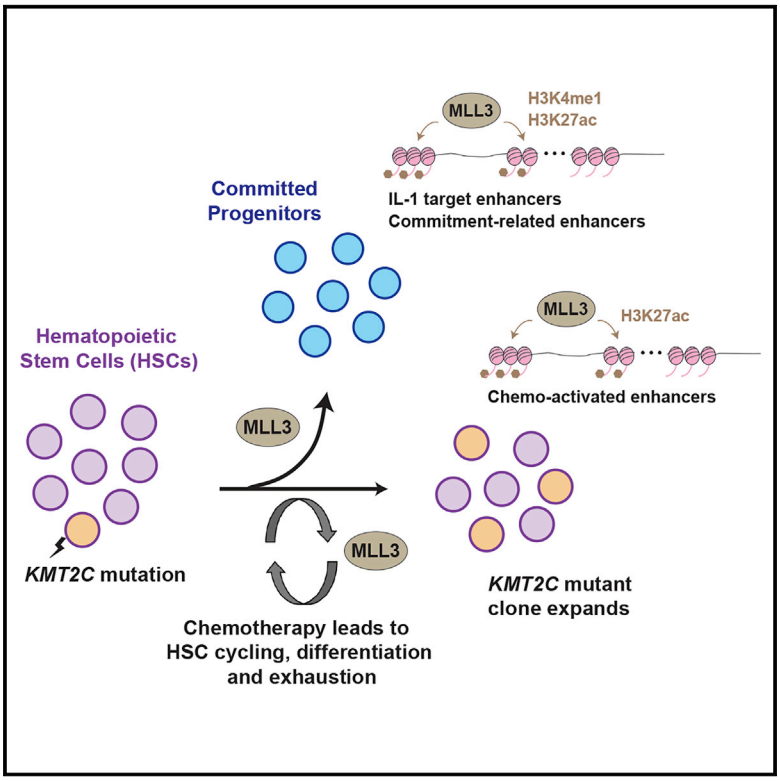

Authors

Ran Chen, Theresa Okeyo-Owuor, Riddhi M. Patel, Emily B. Casey, Andrew S. Cluster, Wei Yang, Jeffrey A. Magee

Correspondence

mageej@wustl.edu

In Brief

Chen et al. use loss-of-function mice to study the role *Kmt2c*/MLL3 in hematopoietic stem cell (HSC) self-renewal. They show that haploid *Kmt2c* deletions impede differentiation when HSCs are driven into cycle by chemotherapy, especially in conjunction with interleukin-1 exposure. This conveys a selective advantage that may promote therapy-related leukemias.

Highlights

- *Kmt2c* deletions enhance HSC self-renewal capacity
- Haploid *Kmt2c* deletions convey a selective advantage to HSCs after chemotherapy
- MLL3 promotes HSC differentiation and enhancer priming in response to IL-1
- MLL3 activates enhancer elements in multiply-divided HSCs

Chen et al., 2021, Cell Reports *34*, 108751
February 16, 2021
https://doi.org/10.1016/j.celrep.2021.108751

CellPress

Cell Reports

CellPress
OPEN ACCESS

Article

Kmt2c mutations enhance HSC self-renewal capacity and convey a selective advantage after chemotherapy

Ran Chen,[1] Theresa Okeyo-Owuor,[1] Riddhi M. Patel,[1] Emily B. Casey,[1] Andrew S. Cluster,[1] Wei Yang,[2] and Jeffrey A. Magee[1,2,3,*]

[1]Department of Pediatrics, Division of Hematology and Oncology, Washington University School of Medicine, 660 S. Euclid Ave., St. Louis, MO 63110, USA

[2]Department of Genetics, Washington University School of Medicine, 660 S. Euclid Ave., St. Louis, MO 63110, USA

[3]Lead contact

*Correspondence: mageej@wustl.edu

https://doi.org/10.1016/j.celrep.2021.108751

SUMMARY

The myeloid tumor suppressor *KMT2C* is recurrently deleted in myelodysplastic syndrome (MDS) and acute myeloid leukemia (AML), particularly therapy-related MDS/AML (t-MDS/t-AML), as part of larger chromosome 7 deletions. Here, we show that *KMT2C* deletions convey a selective advantage to hematopoietic stem cells (HSCs) after chemotherapy treatment that may precipitate t-MDS/t-AML. *Kmt2c* deletions markedly enhance murine HSC self-renewal capacity without altering proliferation rates. Haploid *Kmt2c* deletions convey a selective advantage only when HSCs are driven into cycle by a strong proliferative stimulus, such as chemotherapy. Cycling *Kmt2c*-deficient HSCs fail to differentiate appropriately, particularly in response to interleukin-1. *Kmt2c* deletions mitigate histone methylation/acetylation changes that accrue as HSCs cycle after chemotherapy, and they impair enhancer recruitment during HSC differentiation. These findings help explain why *Kmt2c* deletions are more common in t-MDS/t-AML than in *de novo* AML or clonal hematopoiesis: they selectively protect cycling HSCs from differentiation without inducing HSC proliferation themselves.

INTRODUCTION

Therapy-related myelodysplastic syndrome (t-MDS) and acute myeloid leukemia (t-AML) can arise after patients receive high cumulative doses of chemotherapy for prior, unrelated malignancies. Prognosis for t-MDS/t-AML remains poor even with aggressive modern therapies (Oliai and Schiller, 2020). Thus, it poses one of the most severe long-term complications of chemotherapy. The mutation profiles of t-MDS/t-AML distinguish them from *de novo* AML. Approximately half of all t-MDSs/t-AMLs carry deletions in all or part of chromosome 7, but only 4%–14% of *de novo* AMLs carry chromosome 7 deletions (McNerney et al., 2017; Smith et al., 2003). Chromosome 5 deletions are similarly enriched in t-MDS/t-AML (42% t-MDS/t-AML versus 5%–16% *de novo* AML), as are *TP53* mutations (23%–37% t-MDS/t-AML versus 2%–12% *de novo* AML) (McNerney et al., 2017; Wong et al., 2015). The distinct mutation profiles, coupled with poor survival rates, suggest that t-MDS/t-AML and *de novo* AML arise via distinct mechanisms.

To initiate t-MDS/t-AML, pre-leukemic hematopoietic stem cells (HSCs) and other myeloid progenitors must acquire driver mutations, either prior to chemotherapy or as a consequence of chemotherapy, that convey a selective advantage through the course of additional treatment cycles. A good example of this phenomenon involves *TP53* mutations, which can arise in HSCs prior to therapy and then drive t-MDS/t-AML during and after chemotherapy (Wong et al., 2015). Monosomy 7 (−7) and 7q deletions (del7q) also arise within HSCs and immature myeloid progenitor populations (Will et al., 2012), but less is known about how −7/del7q potentiates t-MDS/t-AML. One possibility is that −7/del7q conveys resistance to DNA damage responses that otherwise limit HSC self-renewal after chemotherapy. A second possibility is that mutations convey resistance to HSC exhaustion, a phenomenon in which self-renewal capacity declines as HSCs undergo multiple self-renewing divisions (Bernitz et al., 2016; Foudi et al., 2009; Qiu et al., 2014; Wilson et al., 2008). DNA damage can contribute to HSC exhaustion (Walter et al., 2015), but other physiological changes, such as mitochondrial dysfunction and epigenetic reprogramming, also restrict self-renewal capacity in multiply-divided HSCs (Beerman et al., 2013; Hinge et al., 2020; Liang et al., 2020). Cycling HSCs must bypass these restrictions to give rise to t-MDS/t-AML.

KMT2C is one of several putative tumor suppressor genes that are recurrently deleted in −7/del7q leukemias, including t-MDS/t-AML (Chen et al., 2014). Mouse models have confirmed that *Kmt2c* is a bona fide myeloid tumor suppressor, because haploid *Kmt2c* deletions can greatly accelerate AML pathogenesis (Chen et al., 2014). Despite this function, *KMT2C* is not

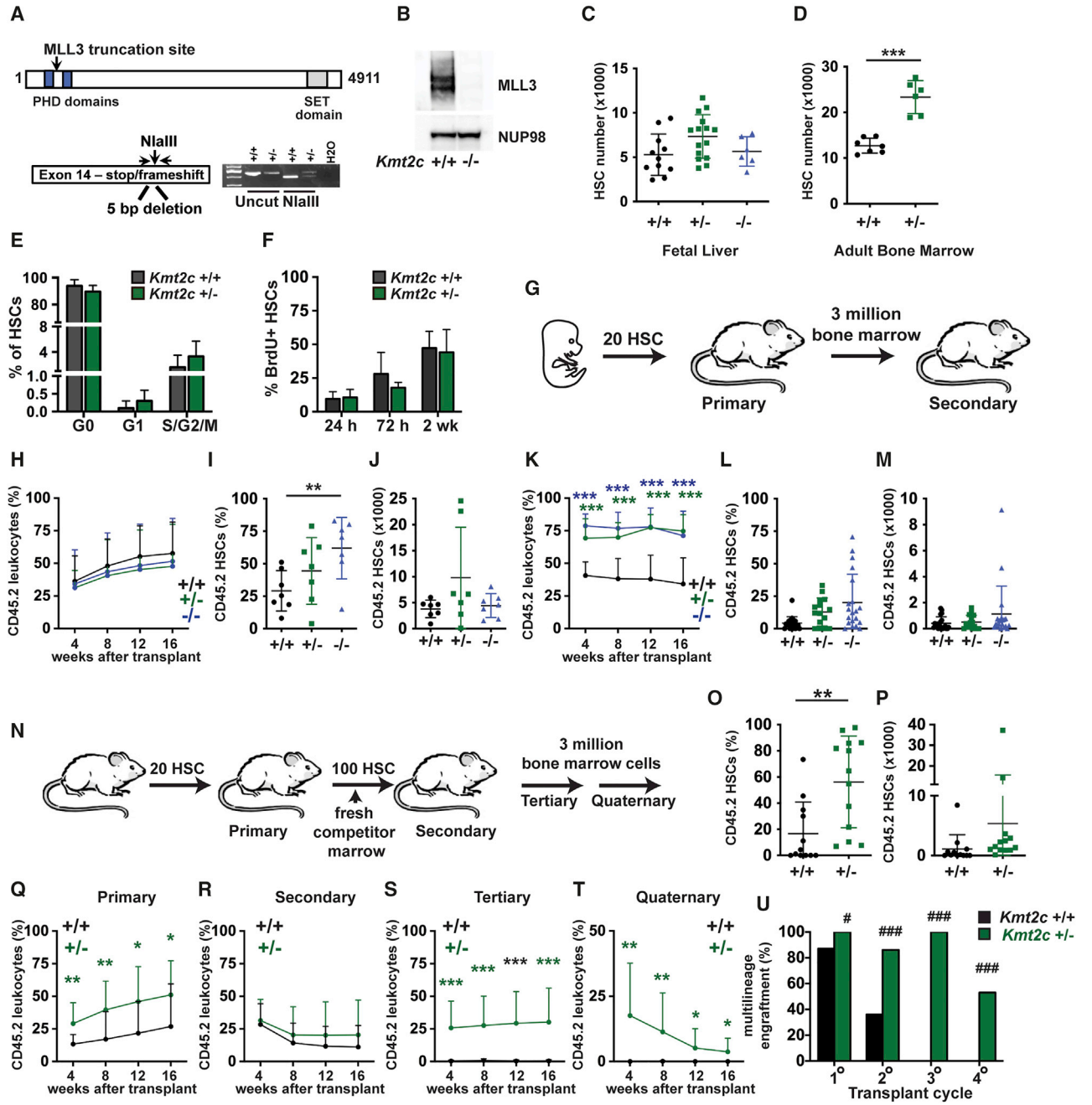

Figure 1. Haploid *Kmt2c* deletion increases HSC numbers and enhances HSC self-renewal capacity

(A) Overview of the germline *Kmt2c* null allele.

(B) MLL3 expression in lysates from wild-type and *Kmt2c*$^{-/-}$ MEFs, as assessed by western blot.

(C and D) HSC numbers in E18.5 fetal livers or 8-week-old adult bone marrow (two hindlimbs) from mice of the indicated *Kmt2c* genotypes. n = 6–15 (fetal) or 6–7 (adult).

(E) Cell-cycle phase distributions of adult *Kmt2c*$^{+/+}$ and *Kmt2c*$^{+/-}$ HSCs as determined by Ki67/DAPI staining. n = 5–6.

(F) HSC BrdU incorporation after 24 h, 72 h, or 2 weeks of BrdU exposure. n = 3–7 per time point and genotype.

(G) Competitive transplantation of fetal HSCs overview.

(H) CD45.2^{+} donor leukocyte chimerism in peripheral blood from primary recipients at the indicated weeks after transplant. n = 14–15 recipients per genotype from at least three independent donors.

(I and J) Donor HSC chimerism and numbers in primary recipient bone marrow 16 weeks after transplantation. n = 7.

(K) Donor leukocyte chimerism in secondary recipients after transplantation of 3 million primary recipient bone marrow cells. n = 15–20 recipients per genotype from at least 5 independent donors.

(legend continued on next page)

recurrently mutated in age-related clonal hematopoiesis, and aged *Kmt2c* knockout mice do not develop MDS or AML (Arcipowski et al., 2016). These observations suggest that haploid *KMT2C* deletions do not, by themselves, convey a strong advantage to affected HSCs. This raises the question of whether *KMT2C* deletions convey a selective advantage only under specific sets of circumstances, such as cumulative chemotherapy cycles that precipitate t-MDS/t-AML.

KMT2C encodes MLL3, a histone methyltransferase that binds enhancer elements and promotes transcription (Hu et al., 2013). MLL3 nucleates COMPASS (complex of proteins associated with Set1) complexes that bind enhancers via interactions with DNA-bound transcription factors and co-factors (Jozwik et al., 2016; Sun et al., 2018; Wang et al., 2018). Once bound, MLL3 monomethylates histone H3, lysine 4 (H3K4me1) to prime enhancers for activation (Herz et al., 2012; Hu et al., 2013; Wang et al., 2016), recruits KDM6A to remove repressive histone H3, lysine 27 tri-methyl marks (H3K27me3) (Wang et al., 2018), recruits CBP/p300 to place activating histone H3, lysine 27 acetyl marks (H3K27ac) (Lai et al., 2017; Wang et al., 2017, 2018), and facilitates long-range interactions between enhancers and their target promoters (Dorighi et al., 2017; Lai et al., 2017; Shilatifard, 2012; Wang et al., 2017; Yan et al., 2018). These observations suggest that MLL3 may help activate differentiation programs in HSCs, similar to what has been described for adipose differentiation (Lee et al., 2013). Alternatively, MLL3 may sensitize HSCs to chemotherapy-induced DNA damage, similar to what has been described in urothelial cells (Lee et al., 2009). In either case, *KMT2C* deletions could convey a selective advantage to HSCs after chemotherapy but before leukemic transformation.

To understand how *Kmt2c*/MLL3 regulates HSC self-renewal, we have generated germline and conditional loss-of-function mice. *Kmt2c* deletions impaired HSC differentiation and conveyed a selective advantage after chemotherapy. This contrasts with a previously described function of *Kmt2d*/MLL4, which is necessary to preserve HSC self-renewal (Santos et al., 2014), and it highlights how highly homologous COMPASS family proteins can have divergent functions in somatic stem cells. At a mechanistic level, we found that *Kmt2c*-deficient HSCs resisted differentiation in response to inflammatory cytokines, such as interleukin-1 (IL-1), but only when they were driven into cycle by other stimuli. Furthermore, *Kmt2c*-deficient HSCs failed to prime and activate enhancers appropriately during HSC differentiation, and they failed to remodel their epigenomes during cumulative division cycles. Thus, the consequences of *Kmt2c* deletion, in HSCs, are largely restricted to contexts in which strong mitogenic stimuli compel HSCs to divide. This context specificity may explain why *KMT2C* deletions arise more frequently in t-MDS/t-AML than in *de novo* AML or age-related clonal hematopoiesis.

RESULTS

Haploid Kmt2c deletion enhances HSC self-renewal capacity

To understand how *Kmt2c* regulates hematopoiesis, we used CRISPR/Cas9 to create a germline premature stop codon in mouse *Kmt2c* exon 14 (Figure 1A). This mutation caused complete loss of protein expression (Figure 1B). $Kmt2c^{-/-}$ mice died at birth yet appeared morphologically normal, consistent with prior studies in which an exon 49 deletion or an intron 33 gene trap insertion led to pulmonary failure and perinatal lethality (Ashokkumar et al., 2020; Lee et al., 2013). We measured HSC numbers ($CD150^{+}CD48^{-}Lineage^{-}c\text{-}kit^{+}Sca1^{+}$; Figure S1A) in wild-type, $Kmt2c^{+/-}$, and $Kmt2c^{-/-}$ embryonic day (E) 18.5 fetal mice and in wild-type and $Kmt2c^{+/-}$ 8-week-old adult mice. HSC numbers were similar in wild-type, $Kmt2c^{+/-}$, and $Kmt2c^{-/-}$ fetal mice (Figure 1C). In contrast, HSC numbers doubled in $Kmt2c^{+/-}$ adult mice relative to controls (Figure 1D). Cell-cycle distributions and bromodeoxyuridine (BrdU) incorporation were similar in wild-type and $Kmt2c^{+/-}$ adult HSCs (Figures 1E and 1F). Thus, haploid *Kmt2c* deletion expanded the adult HSC pool without increasing HSC proliferation rates.

To test whether *Kmt2c* is required for long-term HSC self-renewal, we performed competitive transplantation assays with purified HSCs. Because $Kmt2c^{-/-}$ mice died at birth, we isolated 20 HSCs from wild-type, $Kmt2c^{+/-}$, and $Kmt2c^{-/-}$ E18.5 fetal mice, all on a CD45.2 background, and transplanted them into wild-type CD45.1 recipient mice along with 300,000 wild-type CD45.1 competitor bone marrow cells (Figure 1G). In primary transplants, *Kmt2c* deletion had no effect on peripheral blood reconstitution (Figure 1H; Figure S2A). Donor HSC chimerism was marginally higher in recipients of $Kmt2c^{-/-}$ HSCs than in controls (Figure 1I), but the $Kmt2c^{-/-}$ HSC population did not expand appreciably in numbers (Figure 1J). We next performed secondary transplants with 3 million primary recipient bone marrow cells (Figure 1G). Deletion of one or both *Kmt2c* alleles enhanced reconstitution of all lineages in secondary recipients (Figure 1K; Figure S2B), although $Kmt2c^{-/-}$ HSCs did not expand in numbers relative to controls (Figures 1L and 1M). A similar result was observed when we sorted and transplanted equal numbers of wild-type, $Kmt2c^{+/-}$, and $Kmt2c^{-/-}$ HSCs from the primary recipients (Figures S2C and S2D). The data show the *Kmt2c* deletions enhance HSC repopulating activity without markedly increasing HSC numbers.

We next tested whether haploid *Kmt2c* deletions enhance serial repopulating activity in adult HSCs. We isolated and

(L and M) Donor HSC chimerism and numbers in secondary recipient bone marrow 16 weeks after transplantation. n = 15–20.
(N) Serial transplantation of adult HSCs overview.
(O and P) Donor HSC chimerism and numbers in primary recipient bone marrow. n = 12–13.
(Q–T) $CD45.2^{+}$ donor leukocyte chimerism in peripheral blood from primary, secondary, tertiary, and quaternary recipient mice at the indicated weeks after transplant. n = 14–15 recipients per genotype and transplant cycle from at least three independent donors.
(U) Percentage of mice with multi-lineage CD45.2 chimerism (myeloid, B, and T cell) at 16 weeks after each of the indicated transplant cycles.
For all panels, error bars reflect standard deviation. $^{*}p < 0.05$, $^{**}p < 0.01$, $^{***}p < 0.001$; comparisons were made by two-tailed Student's t test or one-way ANOVA with Holm-Sidak post hoc test (multiple comparisons). (U) $^{\#}p < 0.05$, $^{\#\#\#}p < 0.001$, by Fisher's exact test. See also Figures S1 and S2.

transplanted 20 adult HSCs from 8-week-old wild-type and *Kmt2c*$^{+/-}$ mice, along with 300,000 CD45.1 competitor bone marrow cells (Figure 1N). *Kmt2c*$^{+/-}$ HSCs repopulated primary transplant recipients more effectively than wild-type HSCs, but again with only modest increases in HSC chimerism (Figures 1O–1Q). For secondary transplants, we isolated 100 HSCs from primary recipients and transplanted them with fresh competitor marrow so that secondary recipients received equal numbers of HSCs (Figure 1N). This approach put the donor HSCs at a severe competitive disadvantage relative to the competitor marrow as they had already undergone one round of transplantation, and reconstitution levels were similar for both *Kmt2c* genotypes (Figure 1R). However, *Kmt2c*$^{+/-}$ donor HSCs retained multilineage repopulating activity in tertiary and quaternary transplants, whereas wild-type donor HSCs did not (Figures 1S–1U). Donor *Kmt2c*$^{+/-}$ HSCs were too infrequent to measure after serial rounds of transplantation (data not shown). Collectively, these data show that haploid *Kmt2c* deletions allow HSCs to retain self-renewal capacity through several cycles of transplantation, without triggering metabolic or differentiation programs that lead to HSC exhaustion.

Homozygous Kmt2c deletion modestly expands the adult HSC pool at the expense of more committed progenitor populations

To better study how MLL3 regulates adult hematopoiesis, we generated a conditional *Kmt2c* loss-of-function allele. LoxP sites were placed around exon 3 so that Cre-mediated excision could create a frameshift, premature truncation and complete loss of MLL3 protein expression (Figures 2A and 2B). The conditional allele targeted exon 3, whereas the germline allele targeted exon 14. To confirm that the alleles are functionally equivalent, we deleted a floxed exon 3 allele in the germline with *CMV-Cre*. We then tested whether compound exon 3 and 14 mutations could complement one another and rescue homozygous lethality in late gestation. Crosses of *Kmt2c*$^{+/-}$ (exon 3) and *Kmt2c*$^{+/-}$ (exon 14) parents failed to yield any viable compound heterozygotes at post-natal day (P) 0 (Figure 2C). Thus, the exon 3 and 14 mutations are functionally equivalent, at least with regard to perinatal lethality.

We generated *Kmt2c*$^{f/f}$*; Vav1-Cre* mice (*Kmt2c*$^{\Delta/\Delta}$) to inactivate MLL3 in hematopoietic cells. Spleen weights were marginally enlarged in *Kmt2c*$^{\Delta/+}$ and *Kmt2c*$^{\Delta/\Delta}$ mice (Figure S3A), consistent with a prior observation with MLL3 SET (Su(var)3-9, Enhancer-of-zeste, Trithorax) domain-deficient mice (Arcipowski et al., 2016). Peripheral blood counts were normal in *Kmt2c*$^{\Delta/+}$ and *Kmt2c*$^{\Delta/\Delta}$ mice (Figures S3B–S3D). HSCs expanded to a modest extent in *Kmt2c*$^{\Delta/+}$ and *Kmt2c*$^{\Delta/\Delta}$ mice, consistent with our findings from germline-deleted mice (Figure 2D). Oguro et al. (2013) previously identified two HSC populations based on expression of SLAM surface markers, as well as several distinct populations of multipotent progenitors (MPPs) and committed hematopoietic progenitors (HPCs), and we evaluated these populations after *Kmt2c* deletion (Figures S1A and S3E). Both the deeply quiescent HSC-1 population and a more frequently cycling HSC-2 population expanded in *Kmt2c*$^{\Delta/\Delta}$ mice, as did MPPs (Figure 2E; Figure S3G–S3I). HPC-1 s were depleted in *Kmt2c*$^{\Delta/\Delta}$ mice, but HPC-2 s were not (Figure 2F; Figures S3J and S3K). Pre-granulocyte-monocyte progenitors (pGMs), as defined by Pronk et al. (2007) (Figures S1B and S3F), were depleted in *Kmt2c*$^{\Delta/\Delta}$ mice, but granulocyte-monocyte progenitors (GMPs) and common lymphoid progenitors (CLPs) were not (Figures 2G and 2H; Figure S3L). Immature megakaryocyte and erythroid progenitors (MkP, pre-MegE, and pre-CFU-E) were depleted in *Kmt2c*$^{\Delta/\Delta}$ mice (Figures S3M–S3O), even though more mature CFU-E, red blood cells, and platelets were normal (Figures S3C, S3D, and S3P). Competitive transplantation assays confirmed that *Kmt2c*$^{\Delta/+}$ and *Kmt2c*$^{\Delta/\Delta}$ HSCs repopulate more effectively than wild-type HSCs, consistent with the germline knockout findings (Figures 2I and 2J). Altogether, the data show that modest HSC expansion in *Kmt2c*$^{\Delta/\Delta}$ mice comes at the expense of HPC differentiation. However, by later stages of maturation, the lineages recover their numbers.

Because self-renewal capacity declines when HSCs divide multiple times (Bernitz et al., 2016; Foudi et al., 2009; Qiu et al., 2014; Wilson et al., 2008), we considered that *Kmt2c*$^{\Delta/\Delta}$ HSCs may cycle less frequently than wild-type adult HSCs. BrdU incorporation was equivalent in wild-type and *Kmt2c*$^{\Delta/\Delta}$ mice (Figure 2K; Figure S1C), but the resolution of this assay was limited by the short-term BrdU exposure. To better assess HSC division histories, we used a doxycycline-repressible histone H2B-green fluorescent protein (GFP) allele to monitor HSC divisions over a 14-week period of time, beginning at 8 weeks old (Figure 2L). In this system, GFP-tagged histone H2B was incorporated into the chromatin of all blood cells during development and into adulthood. Doxycycline suppressed H2B-GFP transgene expression, and GFP intensity declined with each cell division. Prior to doxycycline treatment, HSCs expressed high levels of H2B-GFP irrespective of *Kmt2c* genotype (data not shown). After 14 weeks of doxycycline treatment, rapidly dividing HPCs lost H2B-GFP signal, as expected (Figure 2M). In contrast, HSCs retained H2B-GFP signal to varying degrees. Distributions of H2B-GFP-low, -medium and -high HSCs were equivalent for wild-type, *Kmt2c*$^{\Delta/+}$, and *Kmt2c*$^{\Delta/\Delta}$ mice (Figures 2M and 2N; Figure S1D). Thus, *Kmt2c* deletion enhances HSC function and impedes differentiation without altering HSC proliferation rates or dormancy. This suggests that *Kmt2c* deletions might convey a selective advantage primarily in contexts that force quiescent HSCs into cycle.

Chemotherapy conveys a selective advantage to Kmt2c$^{\Delta/+}$ HSCs

To test whether haploid *Kmt2c* deletions convey a selective advantage to non-transplanted HSCs, and whether chemotherapy or inflammatory stress can exacerbate the advantage, we generated *Fgd5-CreER; Kmt2c*$^{f/+}$ mice. *Fgd5-CreER* is expressed exclusively in HSCs (Gazit et al., 2014). We titrated the tamoxifen dose to delete a single *Kmt2c* allele in only ~20% of the HSC pool, as assessed by sorting single HSCs into methylcellulose and genotyping colonies. One week after tamoxifen treatments concluded, we administered one or three cycles of vehicle (phosphate-buffered saline [PBS]), 5-fluorouracil (5-FU), or cyclophosphamide (CY) to drive HSCs into cycle (Figure 3A) (Morrison et al., 1997; Randall and Weissman, 1997). We also treated a cohort of mice with poly-inosine:poly-cytosine (pIpC) to induce type I interferon expression and create inflammatory

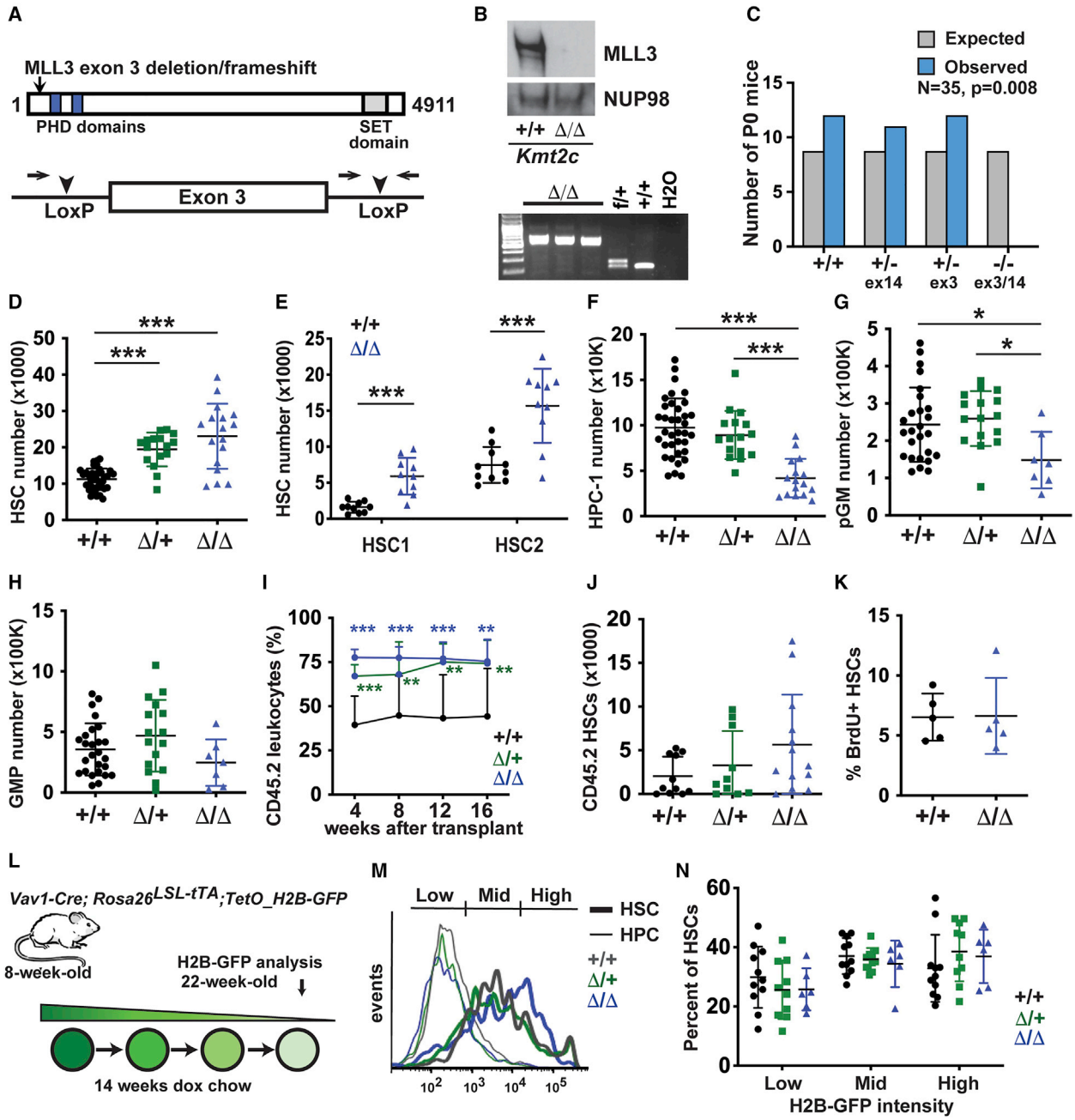

Figure 2. Conditional *Kmt2c* deletion expands the HSC pool at the expense of HPCs

(A) Overview of the conditional *Kmt2c*-flox allele.

(B) Western blot and genotyping PCR showing loss of MLL3 protein expression in $Kmt2c^{\Delta/\Delta}$splenocytes.

(C) Complementation testing of the *Kmt2c* null (exon 14) and $Kmt2c^{flox}$ (exon 3) alleles, as measured by viable offspring after germline $Kmt2c^{flox}$ deletion. Observed and expected allele frequencies were compared by the chi-square test. n = 35.

(D–H) HSC, HPC-1, pGM, and GMP numbers in 8-week-old mice of the indicated *Kmt2c* genotypes (two hindlimbs). n = 7–20.

(I) Peripheral blood $CD45.2^+$ leukocyte chimerism after competitive whole bone marrow transplants. n = 10–13 per genotype from three independent donors.

(J) $CD45.2^+$ HSC numbers in primary recipient bone marrow 16 weeks after transplantation.

(K) Twenty-four-hour BrdU incorporation in wild-type and $Kmt2c^{\Delta/\Delta}$ HSCs. n = 5.

(L) Overview of H2B-GFP pulse-chase experiment.

(M) Representative histograms showing H2B-GFP signal in HSCs and HPCs after 14 weeks of doxycycline exposure.

(N) Percentages of $H2B\text{-}GFP^{High}$, $H2B\text{-}GFP^{Mid}$, and $H2B\text{-}GFP^{Low}$ HSCs after a 14-week doxycycline chase. n = 6–11.

In all panels, error bars reflect standard deviation. *p < 0.05, **p < 0.01, ***p < 0.001; comparisons were made by two-tailed Student's t test or one-way ANOVA with Holm-Sidak post hoc test (multiple comparisons). See also Figures S1 and S3.

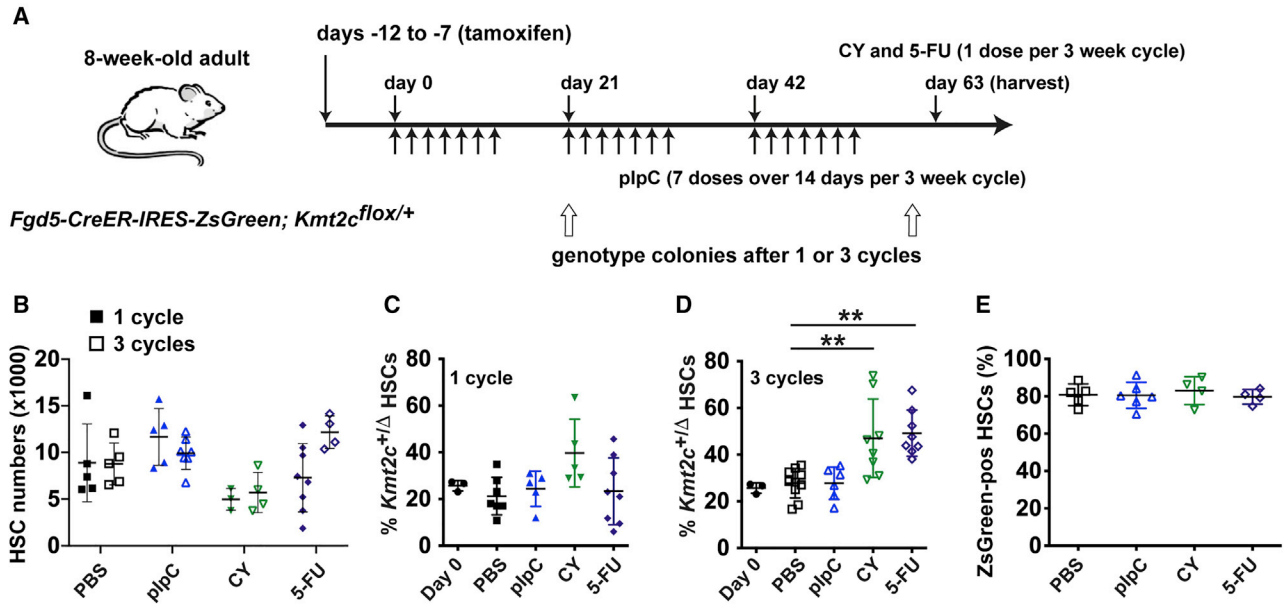

Figure 3. Haploid *Kmt2c* deletion conveys a selective advantage to HSCs that divide after chemotherapy

(A) Overview of the experiment. Arrows indicated treatment days for pIpC, CY, and 5-FU.

(B) HSC numbers in *Fgd5-CreER*; *Kmt2c*$^{flox/+}$ mice after 1 or 3 cycles of the indicated treatments. n = 4–8.

(C and D) Percentage of HSCs with *Kmt2c* deletions after 1 or 3 cycles of the indicated treatments. n = 5–9.

(E) Percentage of ZsGreen-positive HSCs, among all CD150^{+}CD48^{-}LSK cells, after the indicated treatments. n = 4–6. Error bars reflect standard deviation. **p < 0.01, ***p < 0.001; comparisons were made by one-way ANOVA with Holm-Sidak post hoc test.

stress (Figure 3A) (Walter et al., 2015). None of the treatments significantly altered total HSC numbers (Figure 3B), and single cycles of 5-FU, CY, or pIpC did not increase the percentage of *Kmt2c*$^{\Delta/+}$ HSCs relative to PBS controls (Figure 3C). In contrast, three cycles of 5-FU and CY did increase *Kmt2c*$^{\Delta/+}$ HSC frequencies relative to controls, but pIpC did not (Figure 3D). This was not simply due to selection for *Fgd5*-expressing HSCs: the *Fgd5-CreER* allele is linked to an *IRES-ZsGreen* reporter (Gazit et al., 2014), and we did not observe any changes in the percentage of ZsGreen-positive HSCs with 5-FU or CY treatments (Figure 3E). The difference between chemotherapy treatment and pIpC treatment was surprising, and it may reflect a recent observation that pIpC primarily activates a non-repopulating subpopulation of CD150^{+}CD48^{-}LSK cells that does not express *Fgd5* (Bujanover et al., 2018), or pIpC may simply be a weaker mitogenic stimulus than 5-FU or CY. Regardless, the data again show that *Kmt2c*-deleted HSCs can cycle extensively without activating differentiation or exhaustion mechanisms. This conveys a selective advantage, but only in the context of sustained HSC proliferation, as occurs after several cumulative cycles of chemotherapy.

Kmt2c deletion has negligible effects on reactive oxygen species generation and DNA damage

The consequences of *Kmt2c*/MLL3 inactivation in HSCs differ considerably from previously described consequences of *Kmt2d*/MLL4 inactivation. HSC self-renewal capacity increases following *Kmt2c* deletion (Figures 1 and 2), whereas it decreases following *Kmt2d* deletion (Santos et al., 2014). Loss of self-renewal capacity in *Kmt2d*$^{\Delta/\Delta}$ HSCs has been attributed to reduced anti-oxidant gene expression, increased reactive oxygen species (ROS) levels, and elevated DNA damage that promotes differentiation (Santos et al., 2014). We therefore tested whether *Kmt2c* deletion can enhance self-renewal capacity by suppressing ROS and DNA damage after chemotherapy.

We used 2′,7′-dichlorofluorescein diacetate (DCFDA) and γH2Ax staining to measure ROS levels and DNA damage, respectively. We analyzed wild-type and *Kmt2c*$^{\Delta/\Delta}$ HSCs at baseline and 2 days after CY treatment, when the HSCs had entered cycle. We chose CY rather than 5-FU for these experiments because HSC surface marker phenotypes are stable 2 days after CY treatment, in contrast with 5-FU (Morrison et al., 1997; Umemoto et al., 2018). At baseline, we did not observe ROS level changes in *Kmt2c*$^{\Delta/\Delta}$ HSCs (Figures S4A and S4B), After CY treatment, ROS levels were slightly, but significantly, attenuated in *Kmt2c*$^{\Delta/\Delta}$ HSCs (Figures S4A and S4B). DNA damage was similar in wild-type and *Kmt2c*$^{\Delta/\Delta}$ HSCs, irrespective of CY treatment (Figures S4C and S4D). Thus, *Kmt2c* deletion causes only a modest reduction on ROS levels, and it does not reduce DNA damage after CY.

Kmt2c deletion blunts inflammatory programs and induces glutathione-related gene expression in HSCs

To better understand how *Kmt2c*/MLL3 regulates HSC self-renewal and hematopoiesis, we performed RNA sequencing (RNA-seq) with wild-type, *Kmt2c*$^{\Delta/+}$, and *Kmt2c*$^{\Delta/\Delta}$ HSCs, HPC-1 s, pGMs, and GMPs. We identified 328 genes that were expressed lower in *Kmt2c*$^{\Delta/\Delta}$ HSCs as compared with wild-

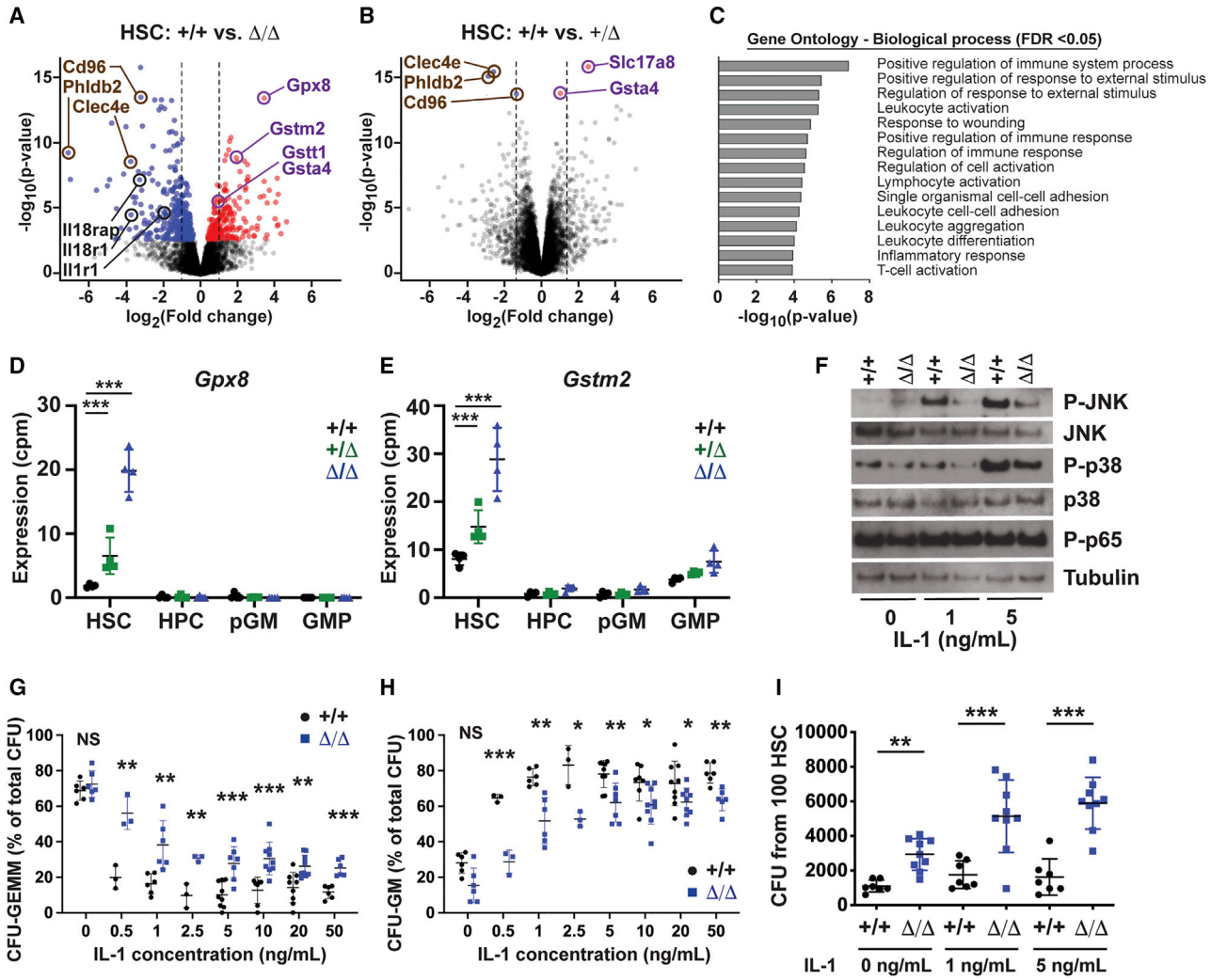

Figure 4. *Kmt2c* deletion reduces sensitivity to IL-1 and enhances antioxidant gene expression in HSCs

(A and B) Volcano plots showing gene expression changes in *Kmt2c*$^{\Delta/\Delta}$ and *Kmt2c*$^{\Delta/+}$ HSCs. Red and blue denote significantly increased or decreased expression after *Kmt2c* deletion (FDR < 0.05). n = 4.

(C) GAGE pathway analysis of genes reduced in *Kmt2c*$^{\Delta/\Delta}$ HSCs.

(D and E) *Gpx8* and *Gstm2* expression in HSCs, HPC-1 s, pGMs, and GMPs. n = 4 per genotype.

(F) Western blots showing JNK, p38, and p65 phosphorylation in HSCs after *ex vivo* IL-1β exposure.

(G and H) CFU-GEMM and CFU-GM percentages for wild-type and *Kmt2c*$^{\Delta/\Delta}$ HSCs plated in the indicated IL-1β concentrations. n = 3–8.

(I) Total CFU activity after 100 wild-type and *Kmt2c*$^{\Delta/\Delta}$ HSCs were cultured for 7 days with IL-1β at the indicated concentration. n = 7–9. Error bars reflect standard deviation.

*p < 0.05, **p < 0.01, ***p < 0.001; comparisons were made by two-tailed Student's t test or one-way ANOVA with Holm-Sidak post hoc test (multiple comparisons). See also Figures S4 and S5 and Table S1.

type (false discovery rate [FDR] < 0.05) and 213 genes that were expressed more highly (Figure 4A). Of these, only five met the same criteria for differential expression in *Kmt2c*$^{\Delta/+}$ HSCs, although 192 met a less stringent criterion of p < 0.05 (Figure 4B; Table S1). There was surprisingly little overlap between genes that were differentially expressed in *Kmt2c*$^{\Delta/\Delta}$ HSCs and those that were differentially expressed in HPC-1 s, pGMs, and GMPs (Figures S5A–S5D). GAGE (generally applicable gene set enrichment) pathway analysis showed reduced expression of genes associated with inflammation, IL-1, and inflammasome signaling in HSCs (Figures 4A and 4C). IL-1 stimulates HSCs to differentiate into myeloid progenitors (Pietras et al., 2016; Rabe et al., 2020). Thus, MLL3 may mediate IL-1-stimulated differentiation.

In addition to the downregulated genes, several glutathione-related genes were upregulated in *Kmt2c*$^{\Delta/+}$ and *Kmt2c*$^{\Delta/\Delta}$ HSCs, relative to wild-type controls, including *Gpx8*, *Gsta4*, *Gstt1*, and *Gstm2* (Figures 4D and 4E; Table S1). These increases were not observed in HPC-1 s, pGMs, or GMPs (Figures 4D and 4E). GPX8 reduces hydrogen peroxide by oxidizing

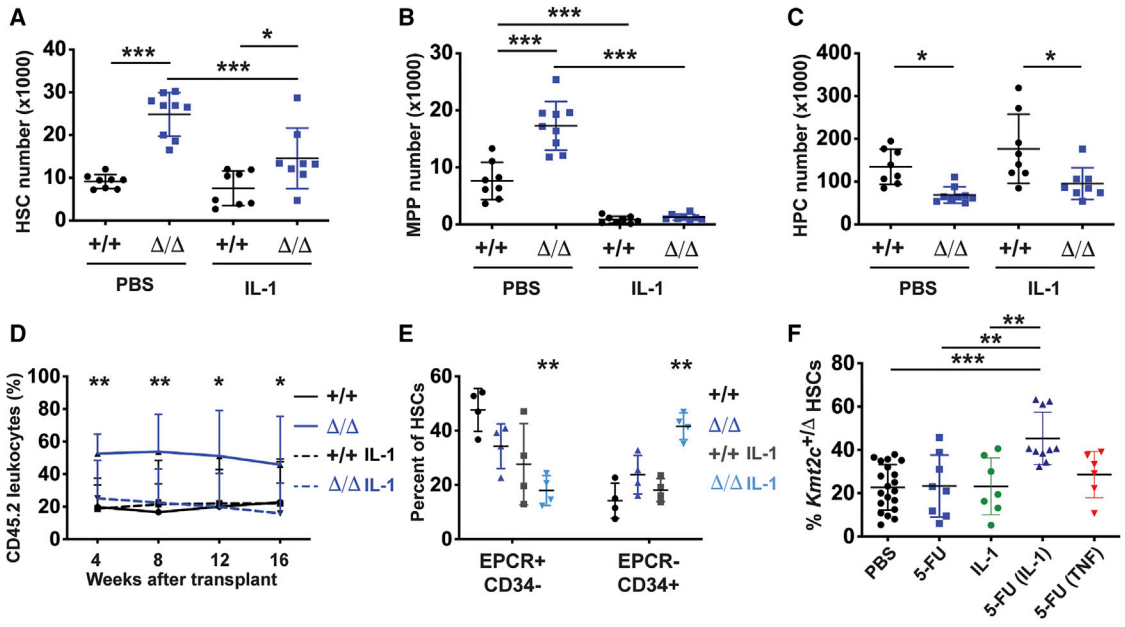

Figure 5. *Kmt2c* deletion impairs IL-1β-driven myeloid differentiation and conveys a selective advantage to cycling, IL-1β-stimulated HSCs

(A–C) HSC, MPP, and HPC numbers in wild-type and *Kmt2c*$^{\Delta/\Delta}$ mice after treatment with PBS or IL-1β for 3 days. n = 8–9.

(D) CD45.2^{+} donor leukocyte chimerism in peripheral blood from primary recipients transplanted with 20 wild-type and *Kmt2c*$^{\Delta/\Delta}$ HSCs, after a 21-day treatment with vehicle (PBS) or IL-1β. n = 10–13.

(E) Phenotypic HSC subpopulations after IL-1β treatment based on EPCR and CD34 expression.

(F) Percent of HSCs with *Kmt2c* deletions after one cycle of PBS or 5-FU, with or without concomitant IL-1β or TNF. n = 6–20. Error bars reflect standard deviation. *p < 0.05, **p < 0.01, ***p < 0.001; comparisons were made by two-tailed Student's t test or one-way ANOVA with Holm-Sidak post hoc test (multiple comparisons).

glutathione, and it regulates calcium flux between the mitochondria and endoplasmic reticulum (Brigelius-Flohé and Maiorino, 2013; Yoboue et al., 2017). The glutathione *S*-transferases (GSTA4, GSTT1, and GSTM2) conjugate glutathione to xenobiotic compounds and mitigate oxidative stress (Ye et al., 2015). These changes contrast with decreases in antioxidant gene expression that occur in *Kmt2d*$^{\Delta/\Delta}$ HSCs (Santos et al., 2014).

MLL3 mediates IL-1-induced myeloid differentiation *in vitro*

Because the RNA-seq data suggest that MLL3 may mediate IL-1-stimulated differentiation, we tested whether *Kmt2c* deletion could impair IL-1 signal transduction or myeloid commitment *in vitro*. To assess signal transduction, we isolated 30,000 HSCs and HPC-1 s from wild-type and *Kmt2c*$^{\Delta/\Delta}$ mice. We incubated the cells for 30 min with 0, 1, or 5 ng/mL recombinant IL-1β. We then performed western blots to assess signal transduction. IL-1β has been shown to activate NF-κB (p65), p38, and JNK pathways. We did not observe changes in p65 phosphorylation, but p38 and JNK phosphorylation were reduced in IL-1β-treated *Kmt2c*$^{\Delta/\Delta}$ HSCs (Figure 4F). These pathways were not suppressed in *Kmt2c*$^{\Delta/\Delta}$ HPCs (Figure S5E). To test whether MLL3 primes HSCs to differentiate in response to IL-1, we sorted single HSCs into methylcellulose supplemented with IL-1β ranging from 0.5 to 50 ng/mL. Consistent with prior work (Pietras et al., 2016), IL-1β exposure significantly reduced multilineage colony formation (CFU-GEMM) and increased granulocyte-monocyte colony formation (CFU-GM), even at low concentrations (Figures 4G and 4H). *Kmt2c* deletion blunted this effect, particularly at low IL-1β concentrations (Figures 4G and 4H).

We next tested whether *Kmt2c* deletion could allow cultured HSCs to retain colony-forming activity, even upon exposure to IL-1β. We sorted 100 HSCs into liquid media supplemented with stem cell factor (SCF), thrombopoietin (TPO), and 0, 1, or 5 ng/mL of IL-1β. We cultured the cells for 7 days and then plated 1% of the culture volume in methylcellulose. Wild-type HSCs yielded similar numbers of colony-forming units (CFUs) after 7 days of exposure to all IL-1β concentrations (Figure 4I). *Kmt2c*$^{\Delta/\Delta}$ HSCs gave rise to more CFUs than wild-type HSCs, and CFUs increased with IL-1β supplementation (Figure 4I). *Kmt2c*$^{\Delta/\Delta}$ HSCs did not fully retain their function as they failed to repopulate irradiated mice after 7 days in culture (data not shown). Nevertheless, the data show that *Kmt2c* deletion impedes differentiation in response to IL-1β *in vitro*.

Quiescent and cycling Kmt2c-deficient HSCs have distinct responses to IL-1 *in vivo*

We next tested whether *Kmt2c* deletion conveys a selective advantage to IL-1β-treated quiescent and dividing HSCs *in vivo*. We first treated adult mice with IL-1β (0.5 μg/day for 3 days). IL-1β treatment unexpectedly reduced *Kmt2c*$^{\Delta/\Delta}$ HSC numbers relative to PBS-treated mice (Figure 5A). A similar reduction was seen after 21 days of treatment (data not shown). MPP numbers were dramatically reduced in IL-1β-treated mice,

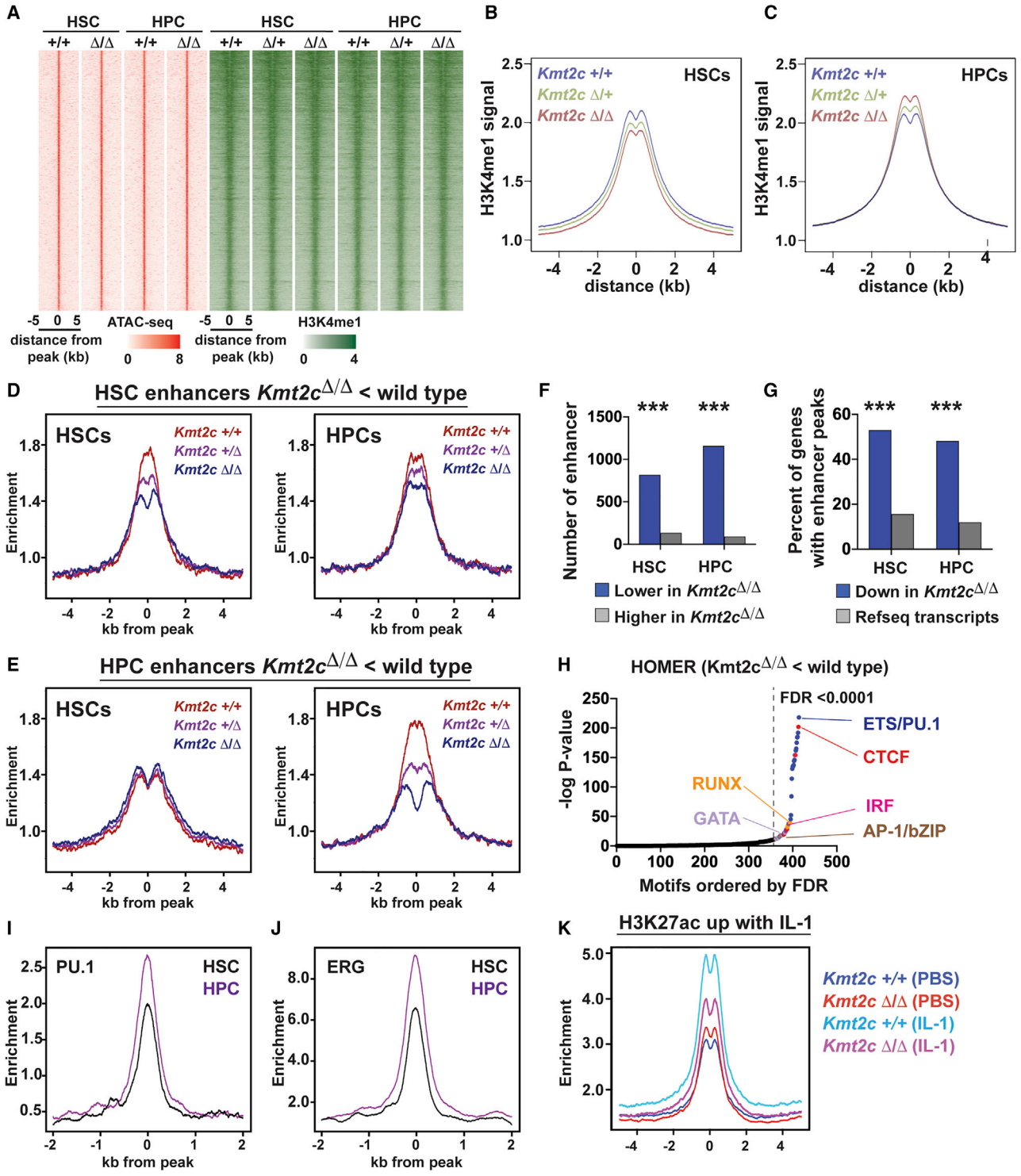

Figure 6. MLL3 promotes enhancer priming and IL-1 target enhancer activation during HSC to HPC differentiation

(A) ATAC-seq (red) and H3K4me1 (green) peaks for all identified HSC and HPC enhancers.

(B and C) Aggregate H3K4me1 levels in wild-type, *Kmt2c*$^{\Delta/+}$, and *Kmt2c*$^{\Delta/\Delta}$ HSCs and HPCs, all enhancers.

(D) Histograms showing H3K4me1 at enhancers with reduced H3K4me1 in *Kmt2c*$^{\Delta/\Delta}$ HSCs relative to wild-type HSCs (HSC enhancers). Data are shown separately for HSCs and HPCs.

(E) Histograms showing H3K4me1 at enhancers with reduced H3K4me1 in *Kmt2c*$^{\Delta/\Delta}$ HPCs relative to wild-type HPCs (HPC enhancers). No *Kmt2c*-dependent changes are observed for these enhancers in HSCs.

(legend continued on next page)

irrespective of *Kmt2c* genotype (Figure 5B). HPC numbers were not affected by IL-1; they were lower in $Kmt2c^{\Delta/\Delta}$ mice in both the PBS and IL-1β treatment groups (Figure 5C). We transplanted 20 HSCs from wild-type and $Kmt2c^{\Delta/\Delta}$ mice after 21 days of PBS or IL-1β treatment and found that IL-1β selectively impaired $Kmt2c^{\Delta/\Delta}$ HSC function (Figure 5D). Prior work has shown that self-renewing HSCs become depleted within the $CD150^{+}CD48^{-}LSK$ population after IL-1 treatment, as evidenced by a reduction in the $EPCR^{+}CD34^{-}$ HSC sub-fraction (Rabe et al., 2020), and we therefore tested whether *Kmt2c* deletion exacerbates this effect. Indeed, after IL-1β treatment, non-self-renewing $EPCR^{-}CD34^{+}$ cells dominated the HSC fraction to a far greater extent in $Kmt2c^{\Delta/\Delta}$ mice than in wild-type mice (Figure 5E). Thus, *Kmt2c* deletion mitigates HSC differentiation *in vitro* (Figure 4), but not *in vivo* (Figure 5), at least not at steady state.

The discrepancy between *in vitro* and *in vivo* responses to IL-1β raised the question of whether this reflects differences in proliferation status. HSCs cycle in culture, but they are usually quiescent in the adult bone marrow. To test this, we treated *Fgd5-CreER*; $Kmt2c^{f/+}$ mice with tamoxifen as in Figure 3. We subsequently treated the mice with a single cycle of 5-FU, IL-1β (0.5 μg/day for 21 days), or both. As before, a single cycle of 5-FU did not increase $Kmt2c^{\Delta/+}$ HSC frequencies relative to undeleted HSCs (Figure 5F). IL-1β treatment also failed to expand the $Kmt2c^{\Delta/+}$ HSC population by itself. However, 5-FU and IL-1β together conveyed a strong selective advantage to $Kmt2c^{\Delta/+}$ HSCs (Figure 5F). This synergy was not observed with another inflammatory cytokine, TNF. The data show that MLL3 promotes HSC differentiation in response to IL-1β, but only when HSCs are driven into cycle by another stimulus, such as culturing or chemotherapy. Inflammatory signaling does not, by itself, convey a selective advantage to $Kmt2c^{\Delta/+}$ HSCs *in vivo*.

MLL3 promotes enhancer recruitment during HSC to HPC differentiation, particularly in response to IL-1

The MLL3 COMPASS complex places H3K4me1 marks at enhancer elements, and it facilitates enhancer activation through CBP/p300-mediated H3K27ac (Herz et al., 2012; Lai et al., 2017). This raised the question of whether MLL3 primes enhancers that mediate differentiation, particularly in response to IL-1. To identify MLL3-regulated enhancer elements, we performed ATAC-seq (Assay for Transposase-Accessible Chromatin using Sequencing) and ChIPmentation (a modified chromatin immunoprecipitation with massively parallel DNA sequencing technique). We identified enhancers as regions of open chromatin with overlapping H3K4me1 peaks (Buenrostro et al., 2015; Schmidl et al., 2015). Altogether, we identified 57,590 enhancers that met these criteria (ATAC-seq peak with overlapping H3K4me1 peak) in either wild-type HSCs or HPC-1 s (Figure 6A). Global H3K4me1 levels were largely unaffected by *Kmt2c* deletions in both the HSC and HPC populations (Figures 6B and 6C; Figure S6A), suggesting that other SET domain proteins, such as MLL4, can monomethylate H3K4 in the absence of MLL3. This raises the question of whether MLL3 regulates a subset of HSC/HPC enhancer elements rather than the global enhancer landscape.

To address this question, we identified enhancers with significantly altered H3K4me1 levels in $Kmt2c^{\Delta/\Delta}$ HSCs and HPCs as compared with wild-type HSCs and HPCs (Figures 6D and 6E). An overwhelming majority of differentially methylated enhancers showed a reduction in H3K4me1 in $Kmt2c^{\Delta/\Delta}$ HSCs/HPCs rather than an increase (Figure 6F). Differentially methylated enhancers were significantly enriched near genes that were also downregulated in $Kmt2c^{\Delta/\Delta}$ HSCs and HPCs (Figure 6G). There was little overlap between enhancers that had significantly lower H3K4me1 in $Kmt2c^{\Delta/\Delta}$ HSCs, relative to wild-type HSCs, and enhancers that had lower H3K4me1 in $Kmt2c^{\Delta/\Delta}$ HPCs, relative to wild-type HPCs (HSC and HPC enhancers, respectively). H3K4me1 priming increased at HPC enhancers during HSC to HPC differentiation (Figure 6E, left versus right panel). This priming failed in the absence of *Kmt2c*/MLL3 (Figure 6E, right). Motif enrichment analysis showed that MLL3-dependent enhancers harbor binding sites for transcription factors that mediate HSC to HPC differentiation, particularly ETS/PU.1, IRF, RUNX, AP-1, and GATA sites. Analysis of previously described ChIP-seq data confirmed that these enhancers bind the ETS domain proteins PU.1 and ERG (Figures 6I and 6J) (Wilson et al., 2016).

We next tested whether IL-1 activates enhancers in an MLL3-dependent manner. We treated wild-type and $Kmt2c^{\Delta/\Delta}$ mice with PBS and IL-1β (0.5 μg/day for 3 days). We isolated HPCs and performed ChIPmentation to measure H3K27ac levels (a mark of active enhancers). IL-1β activated 2,030 enhancers in HPCs, as evidenced by a significant rise in H3K27ac. *Kmt2c* deletion reduced H3K27ac at these enhancers (Figure 6K). Altogether, these data show that MLL3 helps prime HPC enhancers, and it promotes IL-1 target enhancer activation during HSC to HPC differentiation.

MLL3 activates a subset of enhancers when HSCs cycle in response to chemotherapy

Given that *Kmt2c* deletion conveys a selective advantage to cycling HSCs, we tested whether enhancer priming (H3K4me1) and activation (H3K27ac) change in a *Kmt2c*/MLL3-dependent manner as HSCs cycle in response to chemotherapy. We treated wild-type and $Kmt2c^{\Delta/\Delta}$ mice with three cycles of PBS or 5-FU, as in Figure 3A. HSCs were isolated from the bone marrow after

(F) Numbers of enhancers with increased or decreased H3K4me1 levels after *Kmt2c* deletion.
(G) Percent of *Kmt2c*-regulated genes (from Figure 4) with enhancers located within 100 kb of the transcriptional start site. All RefSeq genes are shown as a control. ***$p < 0.0001$ by hypergeometric test.
(H) HOMER motif enrichment showing −log p values for each motif ranked according to decreasing false discovery rate (FDR). Motifs with FDR < 0.0001 are color coded based on unique classes of transcription factor binding domains.
(I and J) PU.1 and ERG binding at HSC and HPC enhancers in HPC-7 cells.
(K) H3K27ac at IL-1 target enhancers in wild-type and $Kmt2c^{\Delta/\Delta}$ HPCs.
See also Figure S6.

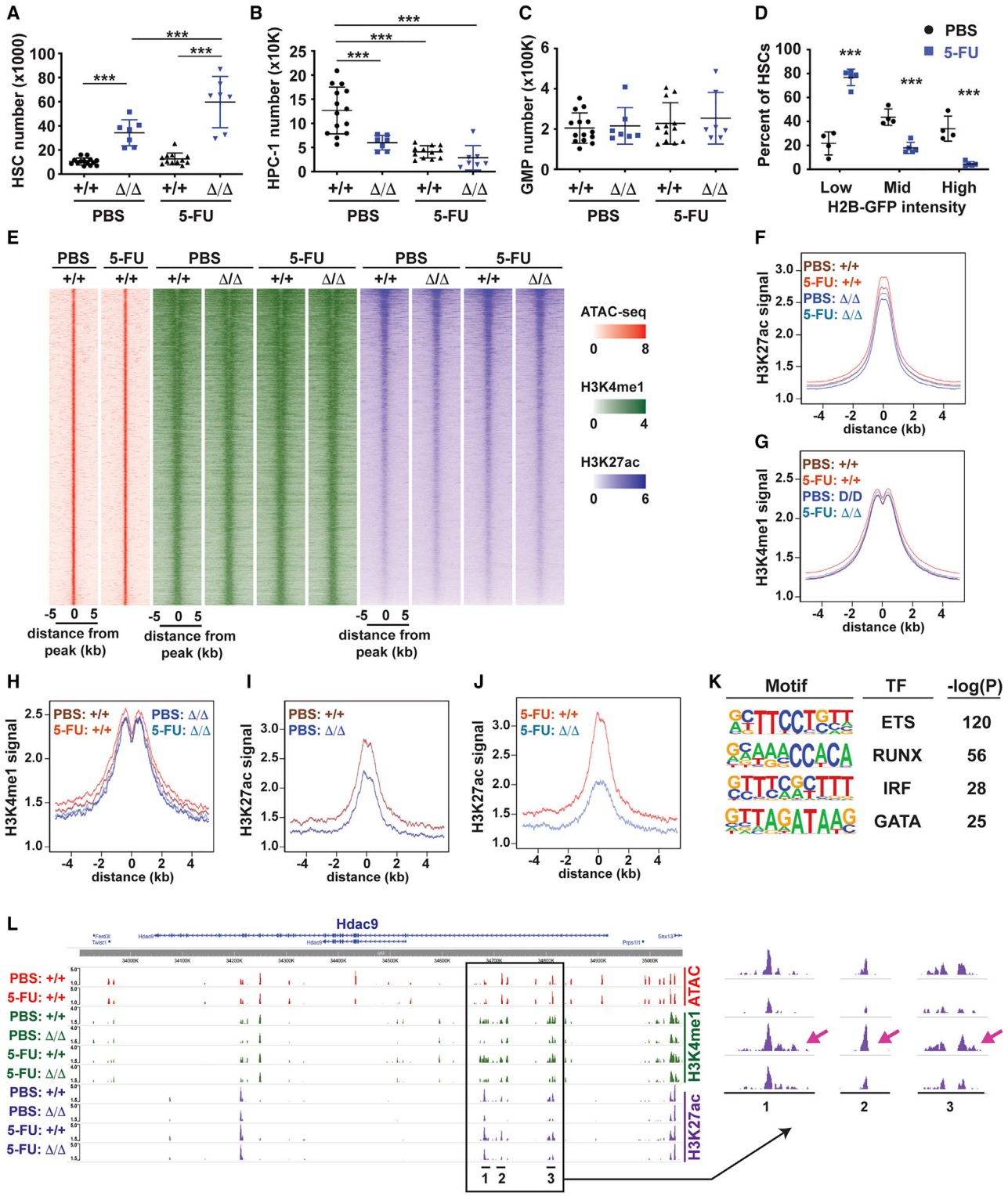

Figure 7. *Kmt2c* deletion mitigates enhancer activation in multiply-divided HSCs

(A–C) HSC, HPC-1, and GMP numbers in wild-type and *Kmt2c*$^{\Delta/\Delta}$ mice treated with three cycles of PBS or 5-FU. n = 7–14. ***p < 0.001 one-way ANOVA with Holm-Sidak post hoc test.

(D) Percentage of H2B-GFP-retaining HSCs after three cycles of PBS or 5-FU treatment. N = 4. ***p < 0.001 by two-tailed Student's t test.

(E) Heatmap showing ATAC-seq, H3K4me1, and H3K27ac at all enhancers in wild-type and *Kmt2c*$^{\Delta/\Delta}$ HSCs after three cycles of PBS or 5-FU treatment.

(legend continued on next page)

the mice had recovered from the third 5-FU cycle (cycle 3, day 21). HSC numbers increased significantly in 5-FU-treated *Kmt2c*$^{\Delta/\Delta}$ mice, relative to vehicle-treated *Kmt2c*$^{\Delta/\Delta}$ mice, but they did not expand in wild-type mice (Figure 7A). HPC-1 numbers declined in 5-FU-treated wild-type mice, but they were already reduced in *Kmt2c*$^{\Delta/\Delta}$ mice and declined no further with 5-FU treatment (Figure 7B). GMP numbers were similar across all genotypes and treatment groups (Figure 7C). H2B-GFP analysis confirmed that HSCs had cycled extensively in the 5-FU treatment group (Figure 7D). These observations are all consistent with our earlier analyses (Figures 2 and 3).

We performed ChIPmentation to identify sites of H3K4me1 and H3K27ac in PBS- and 5-FU-treated wild-type and *Kmt2c*$^{\Delta/\Delta}$ HSCs (Figure 7E). Global H3K4me1 and H3K27ac levels did not change much with 5-FU treatment or *Kmt2c* deletion (Figures 7F and 7G; Figures S6B and S6C). However, we identified 838 enhancers (~2% of all enhancers) that exhibited MLL3-dependent changes in H3K27ac levels. Whereas H3K4me1 levels were similar at these enhancers irrespective of genotype or treatment group (Figure 7H), H3K27ac levels increased after 5-FU treatment, and *Kmt2c* deletion exacerbated the change (Figures 7I and 7J). MLL3-dependent enhancers were enriched for ETS/PU.1, RUNX, IRF, and GATA binding motifs (Figure 7K), and many localized near genes that are downregulated in the absence of *Kmt2c* (e.g., *Hdac9*, *Bach2*, *Dab2*, *Fyb*, *Phldb2*, and *Runx1t1*) (Figure 7L; Figures S7A–S7D). Further studies are needed to determine which MLL3 target genes contribute to HSC exhaustion and why these enhancers are exquisitely dependent on MLL3. Nevertheless, the data show that as HSCs undergo self-renewing divisions after chemotherapy, their epigenomes change, and previously inactive enhancers become active in an MLL3-dependent manner.

DISCUSSION

Our data provide a framework for understanding how *KMT2C* deletions convey a selective advantage in the context of larger chromosome 7q deletions. Prior studies have shown that haploid *KMT2C* deletions accelerate myeloid transformation (Chen et al., 2014). Now we show that it enhances HSC self-renewal capacity, as well. MLL3 primes enhancers for activation during HSC differentiation into HPCs, and it promotes enhancer activation by inflammatory cytokines, most notably IL-1. Furthermore, MLL3 helps reprogram and activate enhancers as HSCs cycle after chemotherapy treatment. *Kmt2c*-mutated HSCs resist these changes and retain self-renewal capacity through cumulative division cycles even as wild-type HSCs become exhausted. This conveys a selective advantage.

Our findings draw an important distinction between mutations that convey a selective advantage after chemotherapy, such as *KMT2C* deletions, and those that convey a selective advantage during aging or inflammation, such as *DNMT3A* or *TET2* mutations. *DNMT3A* mutations suppress HSC cycling and thereby preserve a quiescent HSC pool over decades of life, while simultaneously suppressing differentiation (Challen et al., 2011; Young et al., 2016). *TET2* mutations sensitize HSCs to mitogenic cytokines while simultaneously enhancing self-renewal capacity (Moran-Crusio et al., 2011; Muto et al., 2020). *KMT2C* deletions do neither of these things: HSCs cycle normally, inflammatory target gene expression is suppressed, and the selective advantage becomes most evident when HSCs are driven into cycle by chemotherapy. These observations may help explain why *DNMT3A* and *TET2* mutations are common in age-related clonal hematopoiesis, but *KMT2C* mutations are not (Steensma and Ebert, 2020; Young et al., 2016).

Our findings also highlight divergent functions for *Kmt2c* and its close paralog, *Kmt2d* (MLL4), in HSCs. Prior studies have shown that *Kmt2d* deletion impairs HSC self-renewal by reducing antioxidant gene expression, thereby exacerbating DNA damage (Santos et al., 2014). In contrast, *Kmt2c* deletion increases antioxidant gene expression, has no effect on DNA damage burden even after chemotherapy, and enhances HSC self-renewal capacity. Prior work has shown that in many cell types, such as ESCs, adipocytes, and urothelial cells, *Kmt2c* and *Kmt2d* are at least partially redundant (Dorighi et al., 2017; Lee et al., 2008, 2013). It is therefore interesting that the phenotypes of *Kmt2c*- and *Kmt2d*-deficient HSCs are not only different but also almost reciprocal to one another. This raises the question of whether MLL3 and MLL4 act on shared pathways. For example, it is possible that one or more shared components of the COMPASS complex are rate limiting in HSCs. When MLL3 is lost, stoichiometry could favor MLL4 target gene activation. Likewise, when MLL4 is lost, stoichiometry could favor MLL3 target gene activation. Going forward, it will be important to evaluate compound mutant mice for epistasis and to evaluate the role of other MLL3/4 COMPASS components, such as KDM6A, in HSC self-renewal.

Our data raise additional mechanistic questions. Foremost among these, it is not clear which MLL3 target genes and target enhancers are most responsible for promoting differentiation and impairing self-renewal as HSCs cycle. Furthermore, it is not clear why only a small fraction of all enhancers (~2%) selectively depend on MLL3 and whether their regulation requires SET domain activity. Prior work has shown that N-terminal plant homeodomain (PHD) domains have unique chromatin binding functions that are not evident in MLL4 (Wang et al., 2018), and ongoing studies will test whether these domains mediate MLL3-specific functions in HSCs. Finally, we recognize that *KMT2C* is one of several putative 7q tumor suppressor genes. Thus, the consequences of haploid *Kmt2c* deletion in mice do not capture the full effects of −7/del7q mutations in preleukemic HSCs or t-MDS/t-AML. Future studies must interrogate

(F and G) Aggregate H3K27ac and H3K4me1 levels in wild-type (+/+) and *Kmt2c*-deleted (Δ/Δ) HSCs from mice treated with three cycles of PBS and 5-FU.
(H–J) Aggregate H3K4me1 and H3K27ac levels at MLL3-regulated enhancers (based on H3K27ac) after three cycles of 5-FU treatment.
(K) Top four enriched motifs within MLL3 target enhancers by HOMER.
(L) ATAC-seq, H3K4me1, and H3K27ac tracks at the *Hdac9* locus. The arrow denotes an increase H3K27ac in wild-type HSCs after 5-FU treatment. n = 2–4 (ATAC) and n = 3–6 (H3K4me1, H3K27ac) biological replicates per genotype/cell type/treatment group.
Error bars in (A)–(D) reflect standard deviations. See also Figures S6 and S7 and Table S2.

interactions between *Kmt2c* and other putative 7q tumor suppressors.

STAR★METHODS

Detailed methods are provided in the online version of this paper and include the following:

- KEY RESOURCES TABLE
- RESOURCE AVAILABILITY
  - Lead contact
  - Materials availability
  - Data and code availability
- EXPERIMENTAL MODEL AND SUBJECT DETAILS
- METHOD DETAILS
  - Kmt2c genotyping
  - Flow cytometry
  - Long-term repopulation assays and serial transplantation
  - Western blots
  - H2B-GFP pulse-chase assays
  - Assessment of Kmt2c-deleted HSC frequency after stress
  - BrdU, cell cycle and γH2AX assays
  - DCFDA assays
  - *In vivo* IL-1β responses
  - RNA-seq
  - ATAC-seq and Chipmentation
  - Colony formation assays
- QUANTIFICATION AND STATISTICAL ANALYSIS
  - Statistical comparisons
  - RNA-seq analysis
  - ATAC-seq and ChIPmentation analyses

Supplemental information

Supplemental information can be found online at https://doi.org/10.1016/j.celrep.2021.108751.

ACKNOWLEDGMENTS

This work was supported by grants to J.A.M. from the NHLBI (R01 HL152180 and R01 HL136504), Alex's Lemonade Stand Foundation ('A' Award), Gabrielle's Angel Foundation, The V Foundation, the American Society of Hematology, Hyundai Hope on Wheels, and the Children's Discovery Institute of Washington University and St. Louis Children's Hospital. We thank the Genome Engineering and iPSC Center and the Department of Pathology Micro-injection Core at Washington University for assistance in generating mouse lines. We thank Todd Druley for helpful discussions.

AUTHOR CONTRIBUTIONS

J.A.M. designed and oversaw all experiments, conducted experiments, interpreted data, wrote the manuscript, and secured funding. R.C. conducted experiments, interpreted data, and wrote the manuscript. T.O.-O., R.M.P., E.B.C., and A.S.C. performed experiments and interpreted data. W.Y. performed all bioinformatic analyses. All authors reviewed and edited the manuscript.

DECLARATION OF INTERESTS

The authors declare no competing interests.

Received: September 21, 2020
Revised: December 16, 2020
Accepted: January 25, 2021
Published: February 16, 2021

REFERENCES

Arcipowski, K.M., Bulic, M., Gurbuxani, S., and Licht, J.D. (2016). Loss of Mll3 Catalytic Function Promotes Aberrant Myelopoiesis. PLoS ONE *11*, e0162515.

Ashokkumar, D., Zhang, Q., Much, C., Bledau, A.S., Naumann, R., Alexopoulou, D., Dahl, A., Goveas, N., Fu, J., Anastassiadis, K., et al. (2020). MLL4 is required after implantation, whereas MLL3 becomes essential during late gestation. Development *147*, dev186999.

Beerman, I., Bock, C., Garrison, B.S., Smith, Z.D., Gu, H., Meissner, A., and Rossi, D.J. (2013). Proliferation-dependent alterations of the DNA methylation landscape underlie hematopoietic stem cell aging. Cell Stem Cell *12*, 413–425.

Bernitz, J.M., Kim, H.S., MacArthur, B., Sieburg, H., and Moore, K. (2016). Hematopoietic Stem Cells Count and Remember Self-Renewal Divisions. Cell *167*, 1296–1309.e10.

Brigelius-Flohé, R., and Maiorino, M. (2013). Glutathione peroxidases. Biochim. Biophys. Acta *1830*, 3289–3303.

Buenrostro, J.D., Giresi, P.G., Zaba, L.C., Chang, H.Y., and Greenleaf, W.J. (2013). Transposition of native chromatin for fast and sensitive epigenomic profiling of open chromatin, DNA-binding proteins and nucleosome position. Nat. Methods *10*, 1213–1218.

Buenrostro, J.D., Wu, B., Chang, H.Y., and Greenleaf, W.J. (2015). ATAC-seq: A Method for Assaying Chromatin Accessibility Genome-Wide. Curr. Protoc. Mol. Biol. *109*, 21.29.1–21.29.9.

Bujanover, N., Goldstein, O., Greenshpan, Y., Turgeman, H., Klainberger, A., Scharff, Y., and Gazit, R. (2018). Identification of immune-activated hematopoietic stem cells. Leukemia *32*, 2016–2020.

Challen, G.A., Sun, D., Jeong, M., Luo, M., Jelinek, J., Berg, J.S., Bock, C., Vasanthakumar, A., Gu, H., Xi, Y., et al. (2011). Dnmt3a is essential for hematopoietic stem cell differentiation. Nat. Genet. *44*, 23–31.

Chen, C., Liu, Y., Rappaport, A.R., Kitzing, T., Schultz, N., Zhao, Z., Shroff, A.S., Dickins, R.A., Vakoc, C.R., Bradner, J.E., et al. (2014). MLL3 is a haploinsufficient 7q tumor suppressor in acute myeloid leukemia. Cancer Cell *25*, 652–665.

Corces, M.R., Trevino, A.E., Hamilton, E.G., Greenside, P.G., Sinnott-Armstrong, N.A., Vesuna, S., Satpathy, A.T., Rubin, A.J., Montine, K.S., Wu, B., et al. (2017). An improved ATAC-seq protocol reduces background and enables interrogation of frozen tissues. Nat. Methods *14*, 959–962.

Dobin, A., Davis, C.A., Schlesinger, F., Drenkow, J., Zaleski, C., Jha, S., Batut, P., Chaisson, M., and Gingeras, T.R. (2013). STAR: ultrafast universal RNA-seq aligner. Bioinformatics *29*, 15–21.

Dorighi, K.M., Swigut, T., Henriques, T., Bhanu, N.V., Scruggs, B.S., Nady, N., Still, C.D., 2nd, Garcia, B.A., Adelman, K., and Wysocka, J. (2017). Mll3 and Mll4 Facilitate Enhancer RNA Synthesis and Transcription from Promoters Independently of H3K4 Monomethylation. Mol. Cell *66*, 568–576.e4.

Foudi, A., Hochedlinger, K., Van Buren, D., Schindler, J.W., Jaenisch, R., Carey, V., and Hock, H. (2009). Analysis of histone 2B-GFP retention reveals slowly cycling hematopoietic stem cells. Nat. Biotechnol. *27*, 84–90.

Gazit, R., Mandal, P.K., Ebina, W., Ben-Zvi, A., Nombela-Arrieta, C., Silberstein, L.E., and Rossi, D.J. (2014). Fgd5 identifies hematopoietic stem cells in the murine bone marrow. J. Exp. Med. *211*, 1315–1331.

Heinz, S., Benner, C., Spann, N., Bertolino, E., Lin, Y.C., Laslo, P., Cheng, J.X., Murre, C., Singh, H., and Glass, C.K. (2010). Simple combinations of lineage-determining transcription factors prime cis-regulatory elements required for macrophage and B cell identities. Mol. Cell *38*, 576–589.

Herz, H.M., Mohan, M., Garruss, A.S., Liang, K., Takahashi, Y.H., Mickey, K., Voets, O., Verrijzer, C.P., and Shilatifard, A. (2012). Enhancer-associated H3K4 monomethylation by Trithorax-related, the Drosophila homolog of mammalian Mll3/Mll4. Genes Dev. *26*, 2604–2620.

Hinge, A., He, J., Bartram, J., Javier, J., Xu, J., Fjellman, E., Sesaki, H., Li, T., Yu, J., Wunderlich, M., et al. (2020). Asymmetrically Segregated Mitochondria Provide Cellular Memory of Hematopoietic Stem Cell Replicative History and Drive HSC Attrition. Cell Stem Cell *26*, 420–430.e6.

Hu, D., Gao, X., Morgan, M.A., Herz, H.M., Smith, E.R., and Shilatifard, A. (2013). The MLL3/MLL4 branches of the COMPASS family function as major histone H3K4 monomethylases at enhancers. Mol. Cell. Biol. *33*, 4745–4754.

Joshi-Tope, G., Gillespie, M., Vastrik, I., D'Eustachio, P., Schmidt, E., de Bono, B., Jassal, B., Gopinath, G.R., Wu, G.R., Matthews, L., et al. (2005). Reactome: a knowledgebase of biological pathways. Nucleic Acids Res. *33*, D428–D432.

Jozwik, K.M., Chernukhin, I., Serandour, A.A., Nagarajan, S., and Carroll, J.S. (2016). FOXA1 Directs H3K4 Monomethylation at Enhancers via Recruitment of the Methyltransferase MLL3. Cell Rep. *17*, 2715–2723.

Kundaje, A., Meuleman, W., Ernst, J., Bilenky, M., Yen, A., Heravi-Moussavi, A., Kheradpour, P., Zhang, Z., Wang, J., Ziller, M.J., et al.; Roadmap Epigenomics Consortium (2015). Integrative analysis of 111 reference human epigenomes. Nature *518*, 317–330.

Lai, B., Lee, J.E., Jang, Y., Wang, L., Peng, W., and Ge, K. (2017). MLL3/MLL4 are required for CBP/p300 binding on enhancers and super-enhancer formation in brown adipogenesis. Nucleic Acids Res. *45*, 6388–6403.

Lee, J., Saha, P.K., Yang, Q.H., Lee, S., Park, J.Y., Suh, Y., Lee, S.K., Chan, L., Roeder, R.G., and Lee, J.W. (2008). Targeted inactivation of MLL3 histone H3-Lys-4 methyltransferase activity in the mouse reveals vital roles for MLL3 in adipogenesis. Proc. Natl. Acad. Sci. USA *105*, 19229–19234.

Lee, J., Kim, D.H., Lee, S., Yang, Q.H., Lee, D.K., Lee, S.K., Roeder, R.G., and Lee, J.W. (2009). A tumor suppressive coactivator complex of p53 containing ASC-2 and histone H3-lysine-4 methyltransferase MLL3 or its paralogue MLL4. Proc. Natl. Acad. Sci. USA *106*, 8513–8518.

Lee, J.E., Wang, C., Xu, S., Cho, Y.W., Wang, L., Feng, X., Baldridge, A., Sartorelli, V., Zhuang, L., Peng, W., and Ge, K. (2013). H3K4 mono- and di-methyltransferase MLL4 is required for enhancer activation during cell differentiation. eLife *2*, e01503.

Li, Q., Brown, J.B., Huang, H., and Bickel, P.J. (2011). Measuring reproducibility of high-throughput experiments. Ann. Appl. Stat. *5*, 1752–1779.

Liang, R., Arif, T., Kalmykova, S., Kasianov, A., Lin, M., Menon, V., Qiu, J., Bernitz, J.M., Moore, K., Lin, F., et al. (2020). Restraining Lysosomal Activity Preserves Hematopoietic Stem Cell Quiescence and Potency. Cell Stem Cell *26*, 359–376.e7.

Luo, W., Friedman, M.S., Shedden, K., Hankenson, K.D., and Woolf, P.J. (2009). GAGE: generally applicable gene set enrichment for pathway analysis. BMC Bioinformatics *10*, 161.

McNerney, M.E., Godley, L.A., and Le Beau, M.M. (2017). Therapy-related myeloid neoplasms: when genetics and environment collide. Nat. Rev. Cancer *17*, 513–527.

Moran-Crusio, K., Reavie, L., Shih, A., Abdel-Wahab, O., Ndiaye-Lobry, D., Lobry, C., Figueroa, M.E., Vasanthakumar, A., Patel, J., Zhao, X., et al. (2011). Tet2 loss leads to increased hematopoietic stem cell self-renewal and myeloid transformation. Cancer Cell *20*, 11–24.

Morrison, S.J., Wright, D.E., and Weissman, I.L. (1997). Cyclophosphamide/granulocyte colony-stimulating factor induces hematopoietic stem cells to proliferate prior to mobilization. Proc. Natl. Acad. Sci. USA *94*, 1908–1913.

Muto, T., Walker, C.S., Choi, K., Hueneman, K., Smith, M.A., Gul, Z., Garcia-Manero, G., Ma, A., Zheng, Y., and Starczynowski, D.T. (2020). Adaptive response to inflammation contributes to sustained myelopoiesis and confers a competitive advantage in myelodysplastic syndrome HSCs. Nat. Immunol. *21*, 535–545.

Nakada, D., Saunders, T.L., and Morrison, S.J. (2010). Lkb1 regulates cell cycle and energy metabolism in haematopoietic stem cells. Nature *468*, 653–658.

Oguro, H., Ding, L., and Morrison, S.J. (2013). SLAM family markers resolve functionally distinct subpopulations of hematopoietic stem cells and multipotent progenitors. Cell Stem Cell *13*, 102–116.

Oliai, C., and Schiller, G. (2020). How to address second and therapy-related acute myelogenous leukaemia. Br. J. Haematol. *188*, 116–128.

Pietras, E.M., Mirantes-Barbeito, C., Fong, S., Loeffler, D., Kovtonyuk, L.V., Zhang, S., Lakshminarasimhan, R., Chin, C.P., Techner, J.M., Will, B., et al. (2016). Chronic interleukin-1 exposure drives haematopoietic stem cells towards precocious myeloid differentiation at the expense of self-renewal. Nat. Cell Biol. *18*, 607–618.

Pronk, C.J., Rossi, D.J., Månsson, R., Attema, J.L., Norddahl, G.L., Chan, C.K., Sigvardsson, M., Weissman, I.L., and Bryder, D. (2007). Elucidation of the phenotypic, functional, and molecular topography of a myeloerythroid progenitor cell hierarchy. Cell Stem Cell *1*, 428–442.

Qiu, J., Papatsenko, D., Niu, X., Schaniel, C., and Moore, K. (2014). Divisional history and hematopoietic stem cell function during homeostasis. Stem Cell Reports *2*, 473–490.

Rabe, J.L., Hernandez, G., Chavez, J.S., Mills, T.S., Nerlov, C., and Pietras, E.M. (2020). CD34 and EPCR coordinately enrich functional murine hematopoietic stem cells under normal and inflammatory conditions. Exp. Hematol. *81*, 1–15.e6.

Randall, T.D., and Weissman, I.L. (1997). Phenotypic and functional changes induced at the clonal level in hematopoietic stem cells after 5-fluorouracil treatment. Blood *89*, 3596–3606.

Ritchie, M.E., Phipson, B., Wu, D., Hu, Y., Law, C.W., Shi, W., and Smyth, G.K. (2015). limma powers differential expression analyses for RNA-sequencing and microarray studies. Nucleic Acids Res. *43*, e47.

Santos, M.A., Faryabi, R.B., Ergen, A.V., Day, A.M., Malhowski, A., Canela, A., Onozawa, M., Lee, J.E., Callen, E., Gutierrez-Martinez, P., et al. (2014). DNA-damage-induced differentiation of leukaemic cells as an anti-cancer barrier. Nature *514*, 107–111.

Schmidl, C., Rendeiro, A.F., Sheffield, N.C., and Bock, C. (2015). ChIPmentation: fast, robust, low-input ChIP-seq for histones and transcription factors. Nat. Methods *12*, 963–965.

Shilatifard, A. (2012). The COMPASS family of histone H3K4 methylases: mechanisms of regulation in development and disease pathogenesis. Annu. Rev. Biochem. *81*, 65–95.

Smith, S.M., Le Beau, M.M., Huo, D., Karrison, T., Sobecks, R.M., Anastasi, J., Vardiman, J.W., Rowley, J.D., and Larson, R.A. (2003). Clinical-cytogenetic associations in 306 patients with therapy-related myelodysplasia and myeloid leukemia: the University of Chicago series. Blood *102*, 43–52.

Steensma, D.P., and Ebert, B.L. (2020). Clonal hematopoiesis as a model for premalignant changes during aging. Exp. Hematol. *83*, 48–56.

Subramanian, A., Tamayo, P., Mootha, V.K., Mukherjee, S., Ebert, B.L., Gillette, M.A., Paulovich, A., Pomeroy, S.L., Golub, T.R., Lander, E.S., and Mesirov, J.P. (2005). Gene set enrichment analysis: a knowledge-based approach for interpreting genome-wide expression profiles. Proc. Natl. Acad. Sci. USA *102*, 15545–15550.

Sun, Y., Zhou, B., Mao, F., Xu, J., Miao, H., Zou, Z., Phuc Khoa, L.T., Jang, Y., Cai, S., Witkin, M., et al. (2018). HOXA9 Reprograms the Enhancer Landscape to Promote Leukemogenesis. Cancer Cell *34*, 643–658.e5.

Umemoto, T., Hashimoto, M., Matsumura, T., Nakamura-Ishizu, A., and Suda, T. (2018). Ca^{2+}-mitochondria axis drives cell division in hematopoietic stem cells. J. Exp. Med. *215*, 2097–2113.

Walter, D., Lier, A., Geiselhart, A., Thalheimer, F.B., Huntscha, S., Sobotta, M.C., Moehrle, B., Brocks, D., Bayindir, I., Kaschutnig, P., et al. (2015). Exit from dormancy provokes DNA-damage-induced attrition in haematopoietic stem cells. Nature *520*, 549–552.

Wang, C., Lee, J.E., Lai, B., Macfarlan, T.S., Xu, S., Zhuang, L., Liu, C., Peng, W., and Ge, K. (2016). Enhancer priming by H3K4 methyltransferase MLL4 controls cell fate transition. Proc. Natl. Acad. Sci. USA *113*, 11871–11876.

Wang, S.P., Tang, Z., Chen, C.W., Shimada, M., Koche, R.P., Wang, L.H., Nakadai, T., Chramiec, A., Krivtsov, A.V., Armstrong, S.A., and Roeder, R.G. (2017). A UTX-MLL4-p300 Transcriptional Regulatory Network Coordinately Shapes Active Enhancer Landscapes for Eliciting Transcription. Mol. Cell *67*, 308–321.e6.

Wang, L., Zhao, Z., Ozark, P.A., Fantini, D., Marshall, S.A., Rendleman, E.J., Cozzolino, K.A., Louis, N., He, X., Morgan, M.A., et al. (2018). Resetting the epigenetic balance of Polycomb and COMPASS function at enhancers for cancer therapy. Nat. Med. *24*, 758–769.

Will, B., Zhou, L., Vogler, T.O., Ben-Neriah, S., Schinke, C., Tamari, R., Yu, Y., Bhagat, T.D., Bhattacharyya, S., Barreyro, L., et al. (2012). Stem and progenitor cells in myelodysplastic syndromes show aberrant stage-specific expansion and harbor genetic and epigenetic alterations. Blood *120*, 2076–2086.

Wilson, A., Laurenti, E., Oser, G., van der Wath, R.C., Blanco-Bose, W., Jaworski, M., Offner, S., Dunant, C.F., Eshkind, L., Bockamp, E., et al. (2008). Hematopoietic stem cells reversibly switch from dormancy to self-renewal during homeostasis and repair. Cell *135*, 1118–1129.

Wilson, N.K., Schoenfelder, S., Hannah, R., Sánchez Castillo, M., Schütte, J., Ladopoulos, V., Mitchelmore, J., Goode, D.K., Calero-Nieto, F.J., Moignard, V., et al. (2016). Integrated genome-scale analysis of the transcriptional regulatory landscape in a blood stem/progenitor cell model. Blood *127*, e12–e23.

Wong, T.N., Ramsingh, G., Young, A.L., Miller, C.A., Touma, W., Welch, J.S., Lamprecht, T.L., Shen, D., Hundal, J., Fulton, R.S., et al. (2015). Role of TP53 mutations in the origin and evolution of therapy-related acute myeloid leukaemia. Nature *518*, 552–555.

Yan, J., Chen, S.A., Local, A., Liu, T., Qiu, Y., Dorighi, K.M., Preissl, S., Rivera, C.M., Wang, C., Ye, Z., et al. (2018). Histone H3 lysine 4 monomethylation modulates long-range chromatin interactions at enhancers. Cell Res. *28*, 387.

Ye, Z.W., Zhang, J., Townsend, D.M., and Tew, K.D. (2015). Oxidative stress, redox regulation and diseases of cellular differentiation. Biochim. Biophys. Acta *1850*, 1607–1621.

Yoboue, E.D., Rimessi, A., Anelli, T., Pinton, P., and Sitia, R. (2017). Regulation of Calcium Fluxes by GPX8, a Type-II Transmembrane Peroxidase Enriched at the Mitochondria-Associated Endoplasmic Reticulum Membrane. Antioxid. Redox Signal. *27*, 583–595.

Young, A.L., Challen, G.A., Birmann, B.M., and Druley, T.E. (2016). Clonal haematopoiesis harbouring AML-associated mutations is ubiquitous in healthy adults. Nat. Commun. *7*, 12484.

Zhou, X., Lowdon, R.F., Li, D., Lawson, H.A., Madden, P.A., Costello, J.F., and Wang, T. (2013). Exploring long-range genome interactions using the WashU Epigenome Browser. Nat. Methods *10*, 375–376.

STAR★METHODS

KEY RESOURCES TABLE

REAGENT or RESOURCE	SOURCE	IDENTIFIER
Antibodies		
CD150-PE	Biolegend	115904; RRID: AB_313683
CD48-APC	Biolegend	103412; RRID: AB_571997
Sca-1-PercpCy5.5	Biolegend	108124; RRID: AB_893615
CD201(EPCR)-APC	Biolegend	141505; RRID: AB_ 2561361
CD48-BV711	Biolegend	103439; RRID: AB_2650824
CD2-FITC	Biolegend	100105; RRID: AB_312652
CD3-FITC	Biolegend	100204; RRID: AB_312661
CD8a-FITC	Biolegend	100706; RRID: AB_312745
B220-FITC	Biolegend	103206; RRID: AB_312991
Gr-1-FITC	Biolegend	108406; RRID: AB_313371
Ter119-FITC	Biolegend	116206; RRID: AB_313707
CD2-APC	Biolegend	100111; RRID: AB_2563089
CD3-APC	Biolegend	100235; RRID: AB_2561455
CD8a-APC	Biolegend	100711; RRID: AB_312750
B220-APC	Biolegend	103211; RRID: AB_312996
Gr-1-APC	Biolegend	108411; RRID: AB_313376
Ter119-APC	Biolegend	116211; RRID: AB_313712
CD2-PE-Cy7	Biolegend	300221; RRID: AB_2572065
CD3-PE-Cy7	Biolegend	100219; RRID: AB_1732068
CD8a-PE-Cy7	Biolegend	100721; RRID: AB_312760
B220-PE-Cy7	Biolegend	103221; RRID: AB_313004
Gr-1-PE-Cy7	Biolegend	108415; RRID: AB_313380
Ter119-PE-Cy7	Biolegend	116223; RRID: AB_2137788
CD48-PE-Cy7	Biolegend	103424; RRID: AB_2075049
CD16/32-BV711	Biolegend	101337; RRID: AB_2565637
CD105-APC	Biolegend	120414; RRID: AB_2277914
CD45.1-APC-Cy7	Biolegend	110716; RRID: AB_313505
CD45.2-FITC	Biolegend	109806; RRID: AB_313443
CD45.2-AF700	Biolegend	109822; RRID: AB_493731
CD11b-APC	Biolegend	101212; RRID: AB_312795
Gr-1-PE-Cy7	Biolegend	108416; RRID: AB_313381
B220-PercpCy5.5	Biolegend	103236; RRID: AB_893354
CD41-AF700	Biolegend	133925; RRID: AB_2572129
CD3-PE	Biolegend	100206; RRID: AB_312663
CD135-Biotin	Biolegend	135307; RRID: AB_1953266
CD117-APC-Cy7	Biolegend	105826; RRID: AB_1626278
H2A.X Phospho(Ser139) –AF647	Biolegend	613407; RRID: AB_2114994
CD117-Biotin	Biolegend	135804; RRID: AB_313213
CD117-PE-Cy7	Biolegend	105814; RRID: AB_313223
CD244.2-AF647	Biolegend	133509; RRID: AB_2072854
CD229-Biotin	Biolegend	122903; RRID: AB_830724
CD41-AF700	Biolegend	133925;RRID: AB_2572129

(*Continued on next page*)

Continued

REAGENT or RESOURCE	SOURCE	IDENTIFIER
CD34-FITC	Thermo Fisher	16-0341-85; RRID: AB_468937
H3K4me1	Diagenode	C15410194; RRID: AB_2637078
H3K27ac	Diagenode	C15410196; RRID: AB_2637079
Anti-MLL3	Sigma-Aldrich	ABE1851
Anti-NUP98	Cell Signaling	2288;RRID: AB_561204
P-JNK	Cell Signaling	4688; RRID: AB_823588
P-p38	Cell Signaling	4511; RRID: AB_2139682
P-p65	Cell Signaling	3033;RRID: AB_331284
JNK	Cell Signaling	9252; RRID: AB_2250373
α-Tubulin	Cell Signaling	2144;RRID: AB_2210548
Chemicals, peptides, and recombinant proteins		
Streptavidin-PE-Cy7	Biolegend	405206
Streptavidin-APC-Cy7	Biolegend	405208
Steptavidin-BV711	Biolegend	405241
Mojosort Streptavidin Nanobeads	Biolegend	76447
Tamoxifen	Cayman Chemical	13258
Cyclophosphamide for injection (500mg/vial)	Sandoz	
5-Fluorouracil	Sigma-Aldrich	F6627-5G
Recombinant Murine IL-1β	Peprotech	211-11B
Recombinant Murine TNF-α	Peprotech	315-01A
Bromo-deoxyuridine	Sigma-Aldrich	B5002
Recombinant murine TPO	Peprotech	315-14
Recombinant murine SCF	Peprotech	250-03
Iscove's Modified Dulbecco's Medium	Thermo Fisher Scientific	31980030
MethoCult™ GF M3434	Stem cell technologies	03434
DirectPCR lysis reagent (Mouse Tail)	Viagen	101-T
StemSpan™ SFEM	Stem cell technologies	09650
2′,7′-Dichlorofluorescin diacetate	Sigma-Aldrich	D6883-50MG
Polyinosinic–polycytidylic acid sodium salt	Sigma-Aldrich	P1530
NuPAGE™ LDS Sample Buffer (4X)	Thermo Fisher Scientific	NP0007
SuperSignal™ West Femto Maximum sensitivity Substrate	Thermo Fisher Scientific	34095
Critical commercial assays		
APC BrdU Flow Kit	BD	51-9000019AK
RNeasy Plus Micro Kit	QIAGEN	74034
MinElute Reaction Cleanup Kit	QIAGEN	28204
Illumina Tagment DNA Enzyme and Buffer (Small Kit)	Illumina	20034210
Sera-Mag Speedbeads	Fisher	09-981-123
NEBNext High-Fidelity 2X PCR Master Mix	NEB	M0541S
Coomassie Plus (Bradford) Assay Kit	Thermo	23236
Ampure XP SPRI Beads	Beckman	B23318
NuPage™ 4 to 12% Bis-Tris Gel (10-well)	Thermo Fisher Scientific	NP0335PK2
Deposited data		
ATAC-seq	This paper	GEO: GSE158158
RNA-seq	This paper	GEO: GSE158160
ChIPmentation	This paper	GEO: GSE158159
Series entry (encompassing all datasets)	This paper	GEO: GSE158162

(*Continued on next page*)

Continued

REAGENT or RESOURCE	SOURCE	IDENTIFIER
Experimental models: organisms/strains		
Mouse: C57BL/6J	The Jackson Laboratory	RRID:IMSR_JAX:006965
Mouse: B6;129S4-*Gt(ROSA)26Sor*$^{tm1(rtTA*M2)Jae}$ *Col1a1*$^{tm7(tetO-HIST1H2BJ/GFP)Jae}$/J	The Jackson Laboratory	RRID:IMSR_JAX:016836
Mouse: C57BL/6N-*Fgd5*$^{tm3(cre/ERT2)Djr}$/J	The Jackson Laboratory	RRID:IMSR_JAX:027789
Mouse: B6.Cg-*Commd10*$^{Tg(Vav1-icre)A2Kio}$/J	The Jackson Laboratory	RRID:IMSR_JAX:008610
Mouse: B6.C-Tg(CMV-cre)1Cgn/J	The Jackson Laboratory	RRID:IMSR_JAX:006054
Mouse: *Kmt2c*-null	This paper	N/A
Mouse: *Kmt2c*-flox	This paper	N/A
Oligonucleotides		
Primer for the exon 14 germline *Kmt2c* mutation genotyping: Forward: GTGACTTAATACGACTC ACTATAGGGCCAACAACATACATCTCAGTC	This paper	N/A
Primer for the exon 14 germline *Kmt2c* mutation genotyping: Reverse: TGTATTGCAGGGAAAGT AAATGTT	This paper	N/A
Primer for the exon 3 conditional floxed allele genotyping: Forward: GAACCTGAGGCTGT CGAAGG	This paper	N/A
Primer for the exon 3 conditional floxed allele genotyping: Reverse: AGCCATTAAACTTAGTGAAGACCA	This paper	N/A
Primer for the exon 3 conditional to identify deleted allele: Forward: GCTCCTCCTCTGGCTTCCA AGGTCA	This paper	N/A
Primer for the exon 3 conditional to identify deleted allele: Reverse: AGGGCATCTAATCTGACAGCTGTAAGC	This paper	N/A
ATAC-seq and ChIPmentation primers	Buenrostro et al., 2013	N/A
Software and algorithms		
STAR version 2.0.4b	(Dobin et al., 2013)	https://github.com/alexdobin/STAR
GAGE (Generally Applicable Gene-set Enrichment)	(Luo et al., 2009)	https://bioconductor.org/packages/release/bioc/html/gage.html
Reactome	(Joshi-Tope et al., 2005)	https://reactome.org
limma/voom	(Ritchie et al., 2015)	https://www.bioconductor.org/packages/release/bioc/html/limma.html
ATAC-seq and DNase-seq processing pipeline, v0.3.3	(Kundaje et al., 2015)	https://github.com/kundajelab/atac_dnase_pipelines
AQUAS TF and histone ChIP-seq pipeline, v0.3.3	(Kundaje et al., 2015)	https://github.com/kundajelab/chipseq_pipeline
Bowtie2	Bowtie, v2.2.26	http://bowtie-bio.sourceforge.net/bowtie2/index.shtml
DiffBind	DiffBind	http://www.bioconductor.org/packages/2.13/bioc/html/DiffBind.html
Irreproducible Discovery Rate (IDR)	(Li et al., 2011)	https://www.encodeproject.org/software/idr
MACS2	MACS2, V2.1.0	https://github.com/macs3-project/MACS
HOMER	(Heinz et al., 2010)	http://homer.ucsd.edu/homer/motif
BD FACSDiva	BD	N/A
Flowjo v.10	Treestar	N/A
GraphPad Prism v.8	GraphPad Software	N/A
WashU Epigenome browser	(Zhou et al., 2013)	https://epigenomegateway.wustl.edu

RESOURCE AVAILABILITY

Lead contact

Further information and requests for reagents and resources should be directed to and will be fulfilled by the Lead Contact, Jeffrey Magee (mageej@wustl.edu).

Materials availability

Kmt2c$^{+/-}$ and *Kmt2c*^{flox} mice are available for unrestricted use, upon request, with a standard institutional material transfer agreement.

Data and code availability

The datasets generated during this study are available at Gene Expression Omnibus under the SuperSeries accession GSE158162. SubSeries accession numbers are GSE158158 (ATAC-Seq), GSE158159 (ChIPmentation) and GSE158160 (RNA-seq). No new code was generated for this study.

EXPERIMENTAL MODEL AND SUBJECT DETAILS

Kmt2c$^{+/-}$ and *Kmt2c*^{flox} mice were generated using guide RNAs generated by the Washington University Genome Engineering and iPSC Center. The guide RNAs were complexed with recombinant CAS9 and nucleofected into C57BL/6J embryos by the Washington University Department of Pathology Micro-injection Core. Single strand oligonucleotides were used to insert LoxP sites through homologous recombination. Successfully targeted founder mice were identified by next generation sequencing. Cis-incorporation of the LoxP sites was confirmed by long-range PCR in the founders and linkage of the insertions in F1 progeny. Founders were backcrossed to C57BL/Ka-Thy-1.1 (CD45.2) mice for at least 3 generations prior to use. PCR assays were developed for subsequent genotyping. *Vav1-Cre* – RRID:IMSR_JAX:008610, *Fgd5-CreER* – RRID:IMSR_JAX:027789, *Rosa*$^{LSL\text{-}tTA}$ – RRID:IMSR_JAX:011008, *Col1a1*$^{TetO\_H2B\text{-}GFP}$ – RRID:IMSR_JAX:016836 and *CMV-Cre* – RRID:IMSR_JAX:006054 mice were obtained from the Jackson Laboratory and genotyped with primers described on the Jackson Laboratory website. All experiments were performed with 8-10-week-old adult mice except as indicated in the figure legends (e.g., E18.5 fetal mice). For experiments requiring longitudinal monitoring (e.g., H2B-GFP lineage tracing, chemotherapy treatments), the treatments began 8 weeks after birth. Male and female mice were used equivalently in all experiments. Mice were housed in a standard pathogen free barrier facility. All procedures were performed according to an IACUC approved protocol at Washington University School of Medicine. All mice were healthy and immune competent. All mice were naive to prior procedures, drugs or tests. Cell lines were not used in these studies.

METHOD DETAILS

Kmt2c genotyping

Mice were genotyped by tail biopsies or fetal liver specimen. For the exon 14 germline *Kmt2c* mutation (Figure 1), primers 5′-GTGACTTAATACGACTCACTATAGGGCCAACAACATACATCTCAGTC-3′ and 5′-TGTATTGCAGGGAAAGTAAATGTT-3′ were used to amplify the cut site. The PCR product was then cut with NlaIII to distinguish wild-type and mutant PCR products by size. The NlaIII site was destroyed by the 5-base pair deletion that produced the Kmt2c null allele, and the product therefore ran larger after cutting (Figure 1A). For the exon 3 conditional allele, primers 5′-TCTGGTTGCTTATGGGTTGAT-3′ and 5′-AGCCATTAAACTTAGTGAAGACCA-3′ were used to follow identify the floxed allele after sequencing had been used to confirm that the loxP sites had been correctly inserted in *cis* to one another. Primers 5′-GCTCCTCCTCTGGCTTCCAAGGTCA-3′ and 5′-AGGGCATCTAATCTGACAGCTGTAAGC-3′ were used to identify the deleted allele.

Flow cytometry

Bone marrow cells were obtained by flushing the long bones (tibias and femurs) or by crushing long bones, pelvic bones and vertebrae with a mortar and pestle in calcium and magnesium-free Hank's buffered salt solution (HBSS), supplemented with 2% heat inactivated bovine serum (GIBCO). Fetal and P0 liver cells were obtained by macerating livers with frosted slides. Single cell suspensions were filtered through a 40 μm cell strainer (Fisher). The cells were then stained sequentially, for 20 minutes each, with biotin conjugated anti-CD117 (c-kit; 2B8) and then Streptavidin-conjugated paramagnetic beads (Biolegend). c-kit+ cells were enriched by magnetic selection with an Automacs or LS magnetic columns (Miltenyi Biotec). Cells were stained for flow cytometry using the following antibodies, all of which were from Biolegend except as indicated: CD150 (TC15-12F12.2), CD48 (HM48-1), Sca1 (D7), c-kit (2B8), Ter119 (Ter-119), CD3 (17A2), CD11b (M1/70), Gr1 (RB6-8C5), B220 (RA3-6B2), CD4 (GK1.5), CD8a (53-6.7), CD2 (RM2-5), CD45.1 (A20), CD45.2 (104), surface IgM (RMM-1), CD5 (53-7.3), CD21 (7E9), CD23 (B3B4), CD135 (eBioscience; A2F10), CD105 (MJ7/18), CD41 (MWReg30), CD16/32 (93). Lineage stains for all experiments included CD2, CD3, CD8a, Ter119, B220 and Gr1. Antibodies to CD4 and CD11b were omitted from the lineage stains because they are expressed on fetal HSCs at low levels. The following surface marker phenotypes were used to define cell populations at all ages: HSCs (CD150^{+}, CD48^{-}, Lineage^{-}, Sca1^{+}, c-kit^{+}), HPCs (CD48^{+}, Lineage^{-}, Sca1^{+}, c-kit^{+}), MPP (CD150^{-}, CD48^{-}, Lineage^{-}, Sca1^{+}, c-kit^{+}), HPC-1 (CD150^{-}, CD48^{+},

Lineage$^-$, Sca1$^+$, c-kit$^+$), HPC-2 (CD150$^+$, CD48$^+$, Lineage$^-$, Sca1$^+$, c-kit$^+$), FLK2+ HPC-1 (CD135$^+$, CD150$^-$, CD48$^+$, Lineage$^-$, Sca1$^+$, c-kit$^+$), pGM (Lineage$^-$, Sca1$^-$, c-kit$^+$, CD150$^-$, CD105$^-$, CD16/32$^-$) and GMP (Lineage$^-$, Sca1$^-$, c-kit$^+$, CD150$^-$, CD105$^-$, CD16/32$^+$). Non-viable cells were excluded from analyses by 4',6-diamidino-2-phenylindone (DAPI) staining (1 μg/ml except as indicated below). Flow cytometry was performed on a BD FACSAria Fusion flow cytometer (BD Biosciences).

Long-term repopulation assays and serial transplantation

Eight- to ten-week old C57BL/6Ka-Thy-1.2 (CD45.1) recipient mice were given two doses of 550 rad delivered at least 3 hours apart from a Cesium-137 source. HSCs or unfractionated bone marrow cells were transplanted at the ratios indicated in the text and figures. Cells were injected via the retroorbital sinus. To assess donor chimerism, peripheral blood was obtained from the submandibular veins of recipient mice at the indicated times after transplantation. Blood was subjected to ammonium-chloride lysis of the red blood cells and leukocytes were stained with antibodies to CD45.2, CD45.1, B220, CD3, CD11b and Gr1 to assess multilineage engraftment.

Western blots

To assess MLL3 protein expression, nuclei were isolated from 1 million mouse embryonic fibroblasts (*Kmt2c*$^{+/+}$ and *Kmt2c*$^{-/-}$; Figure 1B) or adult splenocytes (*Kmt2c*$^{+/+}$ and *Kmt2c*$^{f/f}$*; Vav1-Cre*; Figure 2B) in nuclear lysis buffer (10 mM NaCl, 10 mM Tris pH 8.0, 3 mM $MgCl_2$ + COMPLETE protease inhibitor; Sigma). The nuclei were then resuspended in 1x LDS sample buffer (Thermo) plus 1 mM dithiothreitol (DTT). Specimens were heated at 70°C for 10 minutes. Lysates from an equivalent of 100,000 cells were run on NuPage 3%–8% Tris-acetate gel (Thermo) and transferred overnight to PVDF. Membranes were blocked with 5% BSA and incubated with anti-MLL3 (Millipore, ABE1851) or anti-NUP98 (Cell Signaling, 2288) as a loading control. Membranes were washed with Tris buffered saline (TBS) + 0.05% Tween, incubated with HRP-conjugated secondary antibodies (Cell Signaling, 7076 and 7074) and developed with the SuperSignal Femto kit (Thermo). For signal transduction analyses, 30,000 HSCs or HPCs were isolated by flow cytometry as described above. The cells were pelleted in PBS + 0.05% BSA and resuspended in Iscove's Modified Dubelco's Media (IMDM) + 0.05% BSA and the indicated concentrations of IL-1β. The cells were incubated for 30 minutes at 37°C and then pelleted. They were resuspended in 10 μL of cold PBS, transferred to 10% Trichloroacetic acid, and precipitated by centrifugation. The precipitates were washed twice with acetone and resuspended in solubilization buffer (9M urea, 2% Triton X-100, 1% DTT). LDS sample buffer (Thermo) was subsequently added to 1x final concentration and the specimen was heated at 70°C for 10 minutes. Samples were run on 4%–12% NuPage Bis-Tris gels (Thermo) and processed as described above. Primary antibodies to P-JNK (Cell Signaling, 4688), P-p38 (Cell Signaling, 4511), P-p65 (Cell Signaling, 3033), JNK (Cell Signaling, 9252), p38 (Cell Signaling, 9212) and alpha-tubulin (Cell Signaling, 2144) were added in succession. After each analysis, the membrane was stripped (1% sodium dodecyl sulfate, 25 mM glycine pH 2.0).

H2B-GFP pulse-chase assays

Vav1-Cre, Rosa$^{LSL\text{-}tTA}$, and *Col1a1*$^{TetO\_H2B\text{-}GFP}$ mice were crossed with *Kmt2c*^{flox} mice to generate the alleles indicated in the text. Mice were fed doxycycline chow (200 ppm, Bioserv) beginning at 8 weeks after birth to suppress H2B-GFP expression. HSCs were then isolated and analyzed as described above.

Assessment of Kmt2c-deleted HSC frequency after stress

Eight-week-old *Fgd5-CreER; Kmt2c*$^{f/+}$ mice were treated with tamoxifen (Cayman Chemical) at 100 mg/kg/day for five days. The tamoxifen was administered in corn oil by intraperitoneal injection. This dose was established empirically, based on our goal of deleting the *Kmt2c*^{flox} allele in approximately 20% of HSCs. After tamoxifen treatment, the mice were given 7 days to recover. They were treated intraperitoneally with PBS, 5-FU (150 mg/kg), CY (200 mg/kg) or pIpC (20 μg every other day; Sigma). Mice were treated on the schedules indicated in Figure 3. When IL-1β was administered (Figure 6F), mice were given 0.5 μg of IL-1β (Peprotech) in 100 μL PBS with 0.1% BSA, intraperitoneally once daily for 21 days beginning immediately after 5-FU treatment.

To measure deletion frequencies, single ZsGreen-positive HSCs were sorted into individual wells of a 96-well plate that contained MethoCult GF M3434 methylcellulose media (Stem Cell Technologies). Colonies were isolated 12 days later by washing the well with PBS, pelleting cells and lysing with Direct PCR lysis reagent (Viagen). Genotyping was performed as described above. In the absence of tamoxifen treatment (i.e., – vehicle only), we did not observe any *Kmt2c*-deleted HSCs even after three cycles of 5-FU (data not shown).

BrdU, cell cycle and γH2AX assays

Bromo-deoxyuridine (BrdU; Sigma) was administered by intraperitoneal injection (100 mg/kg/dose) once, and mice were then fed water containing 0.8 mg/mL BrdU for the next 24 hours. HSCs were stained and enriched by c-kit selection as described above. BrdU incorporation was measured by flow cytometry using the APC BrdU Flow Kit (BD Biosciences). For cell cycle and γH2AX analyses, HSCs were stained and enriched by c-kit selection as described above. They were then fixed and permeabilized with cytofix/cytoperm buffer (BD Biosciences), washed, and incubated with streptavidin-PE-CY7 along with Ki67- or γH2AX-AF647 antibodies. Cells were then washed, stained with DAPI (20 μg/mL), and analyzed by flow cytometry.

DCFDA assays

DCFDA staining was performed as described previously (Nakada et al., 2010). Bone marrow was isolated, c-kit enriched and stained as described above, leaving the FITC channel available for DCFDA analysis. We then incubated 2 million stained cells with 5 μM DCFDA (Sigma) for 15 minutes at 37°C. The cells were washed once with staining media, re-suspended in DAPI-containing staining media and immediately analyzed by flow cytometry.

In vivo IL-1β responses

To assess HSC numbers and function after IL-1 treatment, adult mice were treated with PBS or recombinant mouse IL-1β (Peprotech) at 0.5 μg/dose (in 100 μL PBS with 0.1% BSA, intraperitoneally) for 3 or 21 days as previously described (Pietras et al., 2016). Bone marrow was then harvested for analysis and transplantation as described above. To identify compare IL-1 target gene expression in wild-type and *Kmt2c*$^{\Delta/\Delta}$HSCs, we treated mice for three days with IL-1β (0.5 μg/dose intraperitoneally) and then isolated HSCs for RNaseq as described below.

RNA-seq

For each replicate, 10,000 HSCs, HPCs, pGMs or GMPs of the indicated genotypes were double sorted into PBS with 0.1% BSA. Cells were pelleted by centrifugation and resuspended in RLT-plus RNA lysis buffer (QIAGEN). RNA was isolated with RNAeasy micro-plus columns (QIAGEN). RNaseq libraries were generated with Clontech SMRTer kits, and sequencing was performed on a HiSeq3000.

ATAC-seq and Chipmentation

For ATAC-seq, 50,000 HSCs or HPCs of the indicated *Kmt2c* genotypes and treatment groups were double sorted into PBS + 0.1% BSA. At least 3 independent replicates were analyzed per time point and population, with each replicate utilizing cells from multiple mice. Cells were processed, and libraries were generated, using the method described by Corces et al. (2017). Library amplification was performed using barcoded primers as described by Buenrostro et al. (2013). After library amplification, fragments were size selected with SPRI beads (Beckman Coulter) with ratios of 0.9x and 1.8x for right- and left-sided selection. Sequencing was performed on a HiSeq2500.

For ChIPmentation assays, 30,000 HSCs or HPCs of the indicated *Kmt2c* genotypes and treatment groups were double sorted into PBS + 0.1% BSA. ChIPmentation was performed as described by Schmidl et al. (2015). Sonication was performed with a Covaris E220 using empirically defined setting (Peak incident power 105, duty factor 2%, cycles per burst 200, duration 840 s). ChIP-seq grade H3K4me1 and H3K27ac antibodies were purchased from Diagenode. Library amplification was performed using barcoded primers as described by Buenrostro et al. (2013). After library amplification, fragments were size selected with SPRI beads with ratios of 0.65x and 0.9x for right- and left-sided selection. Sequencing was performed on a HiSeq2500.

Colony formation assays

For CFU-assays in which we assessed colony morphology in the presence or absence of IL-1β, we plated 150 freshly sorted HSCs in 1.5 mL of MethoCult GF M3434 media, supplemented with Penicillin-Streptomycin and IL-1β at the indicated concentrations. Colonies were scored 12 days later by an observer blinded to treatment group and genotype.

For assays in which HSCs were cultured *ex vivo* culture followed by colony formation assays (Figure 6C), 100 HSCs from wild-type or *Kmt2c*$^{\Delta/\Delta}$mice were sorted directly into 96-well plates and were grown in StemSpan SFEM (Stem Cell Technologies) supplemented with Penicillin-Streptomycin (GIBCO), recombinant TPO (100 ng/ml; Peprotech), recombinant SCF (100 ng/ml; Peprotech), and IL-1β at the indicated concentrations. The culture cells were counted after 7 days. We then transferred 1% of the culture volume to MethoCult GF M3434 and scored colonies as described above.

QUANTIFICATION AND STATISTICAL ANALYSIS

Statistical comparisons

Group sizes and statistical tests are indicated in the text, with the exception of the bioinformatic analyses that are described below. In all figures, error bars indicate standard deviations. Sample sizes and numbers of replicates are indicated in the figure legends. In all cases in which multiple comparisons were made, a Holm-Sidak posthoc test was used to correct for multiple comparisons. CFU assays were performed blinded as described above. All other comparisons were unblinded.

RNA-seq analysis

Sequences were aligned to the mouse genome (Ensembl release 76 top-level assembly) using STAR version 2.0.4b (Dobin et al., 2013). Linear modeling (limma/voom) was used to compare gene expression across samples (Ritchie et al., 2015). False discovery rates were calculated using the Benjamini and Hochberg method. Pathway analysis was performed with Generally Applicable Gene-set Enrichment (Luo et al., 2009) or Gene Set Enrichment Analysis (Subramanian et al., 2005) or Reactome (Joshi-Tope et al., 2005). Heatmaps for visualizing RNA-seq data were generated with the Spotfire Omics package. RNA-seq data can be accessed from Gene Expression Omnibus (GSE158160).

ATAC-seq and ChIPmentation analyses

ATAC-seq reads were demultiplexed and mapped to mm10 using bowtie2. Peaks were identified and ChIP-seq coverage tracks were generated with MACS2 using the ATAC-seq and DNase-seq processing pipeline developed by the Kundaje lab (https://github.com/kundajelab/atac_dnase_pipelines, Version 0.3.3) (Kundaje et al., 2015). Consistency among replicates was assessed based on Irreproducible Discovery Rates (Li et al., 2011). Differential binding peaks were identified with the R package DiffBind (FDR < 0.1). Signal tracks were visualized with the WashU Epigenome browser (Zhou et al., 2013).

ChIPmentation Reads were demultiplexed and mapped to mm10. Signal enrichment was normalized to the corresponding input samples that were sequenced on each independent run. Peaks were identified and ChIP-seq coverage tracks were generated with MACS2 using the AQUAS TF and histone ChIP-seq pipeline with the "histone" option (https://github.com/kundajelab/chipseq_pipeline, version 0.3.3) (Kundaje et al., 2015). Differential binding peaks were identified with the R package DiffBind (FDR < 0.1). Signal tracks were visualized with the WashU Epigenome browser (Zhou et al., 2013). HOMER was used to identify transcription factor binding sites that were enriched within MLL3-regulated enhancers (Heinz et al., 2010).

ATAC-seq and Chipmentation data can be accessed from Gene Expression Omnibus (GSE158158 and GSE158159, respectively).

Cell Reports, Volume *34*

Supplemental Information

Kmt2c mutations enhance HSC self-renewal capacity and convey a selective advantage after chemotherapy

Ran Chen, Theresa Okeyo-Owuor, Riddhi M. Patel, Emily B. Casey, Andrew S. Cluster, Wei Yang, and Jeffrey A. Magee

Supplemental figures and legends

Figure S1

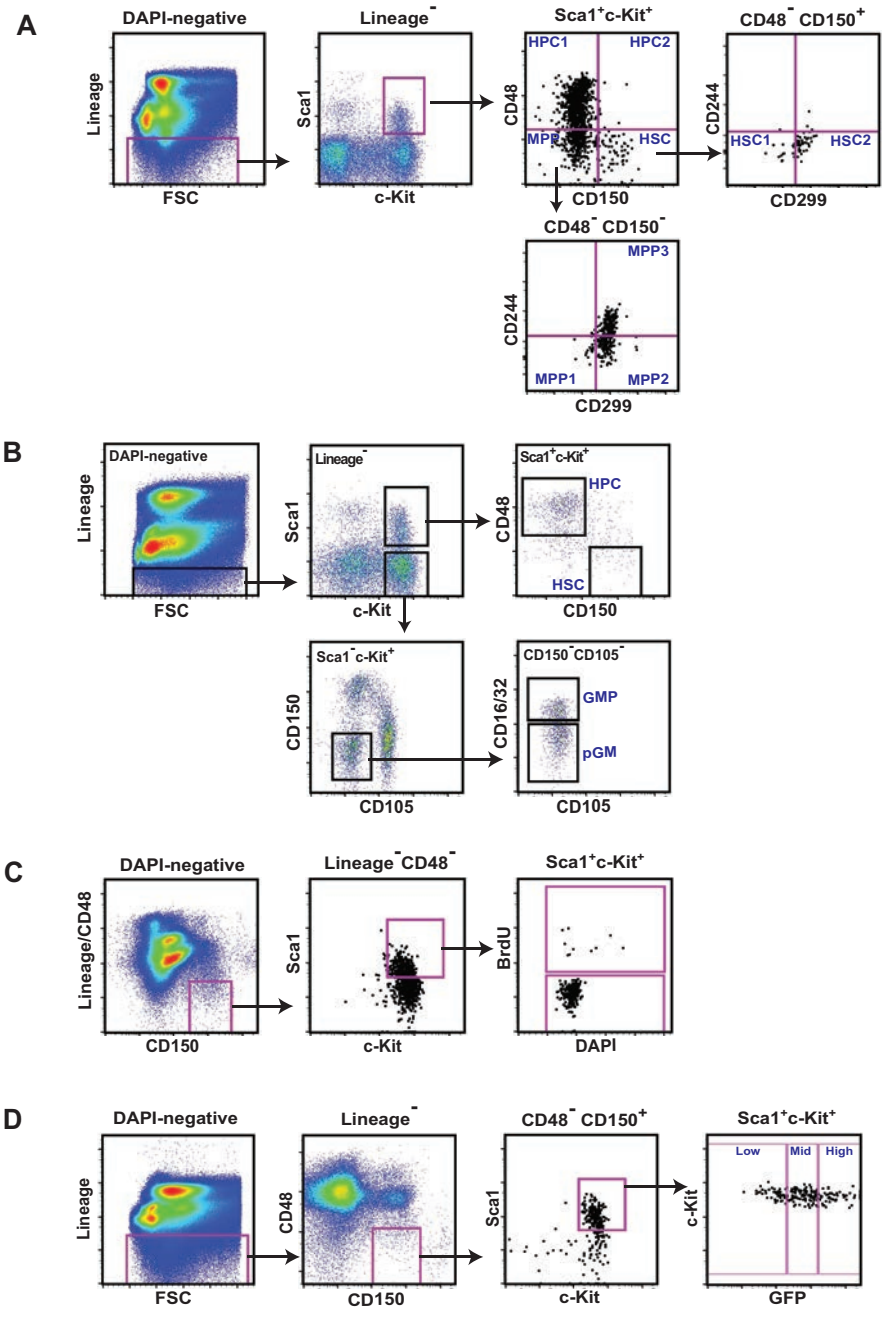

Figure S1 (related to Figures 1 and 2). Gating strategies for populations analyzed in wild type and *Kmt2c*$^{\Delta/\Delta}$ mice. (A) Representative flow plots and gating strategies for HSC, MPP and HPC subpopulations as defined by Oguro et al. (B) Representative flow plots and gating strategies for pGM and GMP populations as defined by Pronk et al. (C) Gating strategy for BrdU incorporation assays in HSCs. (D) Representative flow plots and gating strategy for H2B-GFP assays.

Figure S2

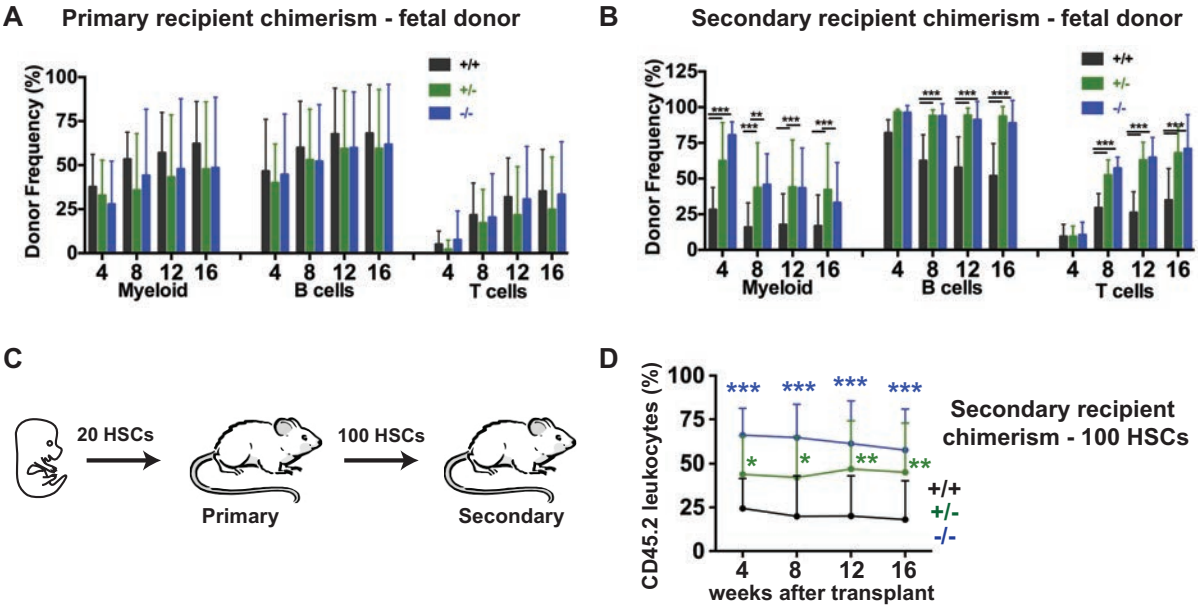

Figure S2 (related to Figure 1). Peripheral blood chimerism after fetal HSC transplants. (A, B) CD45.2 chimerism in peripheral myeloid, B- and T-cell populations in primary and secondary recipient at the indicated weeks after transplant, for the indicated genotypes. n=14-15 recipients per genotype from at least three independent donors. (C) Overview of an alternative approach to secondary transplants in which 100 sorted CD45.2^{+} HSCs (from primary recipients) were transplanted into secondary recipients with 300,000 competitor bone marrow cells. (D) CD45.2 chimerism in secondary recipients that received 100 HSCs. For all panels, error bars reflect standard deviation. *p<0.05, **p<0.01, ***p<0.001; comparisons were made by two-tailed student's t-test (single comparisons) or one-way ANOVA with Holm-Sidak post-hoc test (multiple comparisons).

Figure S3

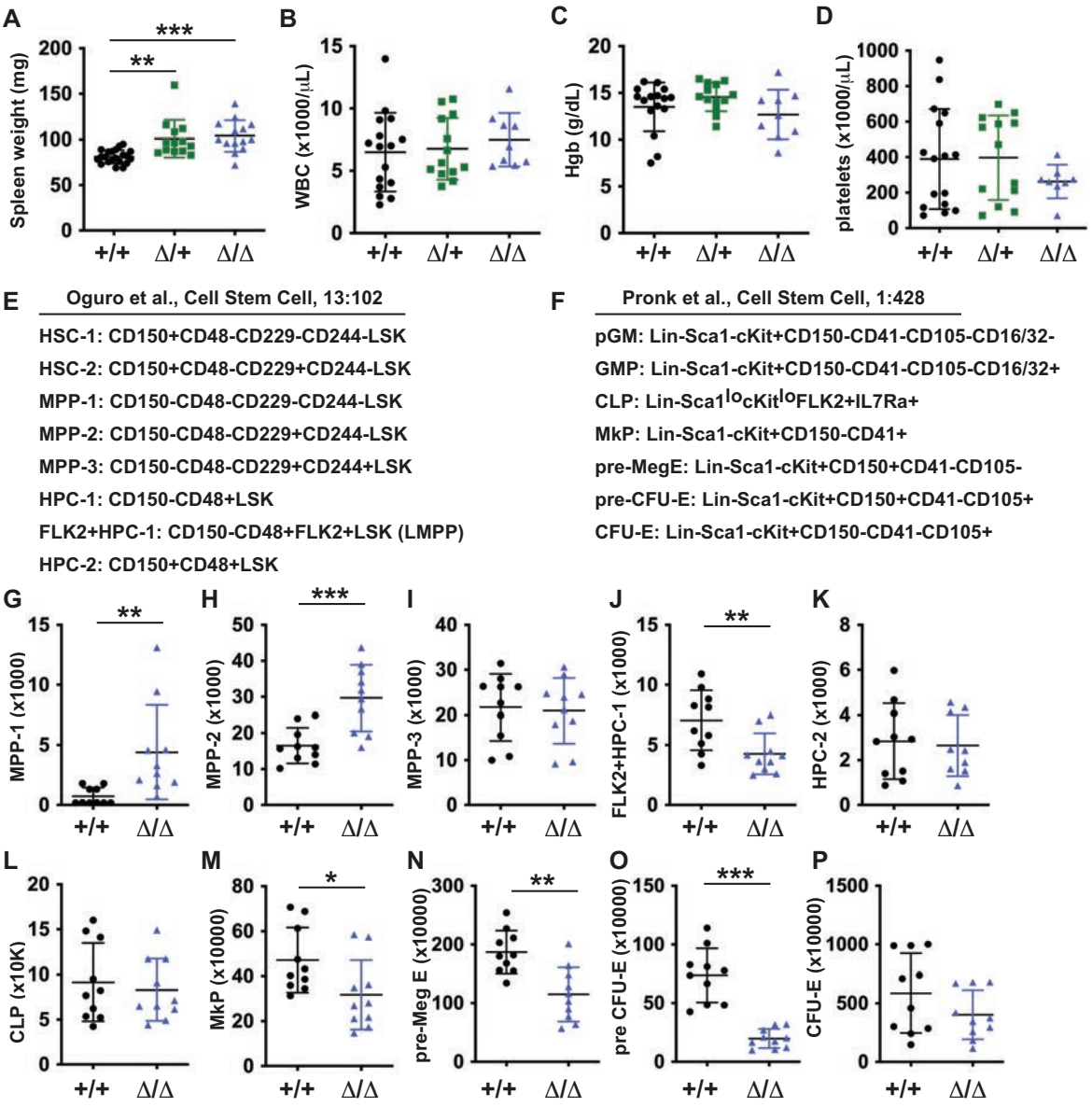

Figure S3 (related to Figure 2). Analysis of hematopoiesis after conditional *Kmt2c* deletion. (A-D) The spleen weights, white blood cell counts, hemoglobin (Hgb) and platelet counts in 8-week-old wild type, $Kmt2c^{\Delta/+}$ and $Kmt2c^{\Delta/\Delta}$ mice. (E, F) Surface marker phenotypes for HSC, MPP, HPC and myeloid progenitor sub-populations that were used in these analyses. See Figure S1 for representative gates. (G-P) Absolute numbers of the indicated HSC, MPP, HPC and myeloid progenitor sub-populations in bone marrow (two hind limbs) from wild type and $Kmt2c^{\Delta/\Delta}$ mice. n=10. Error bars reflect standard deviations. *p<0.05, **p<0.01, ***p<0.001 by two-tailed Student's t-test.

Figure S4

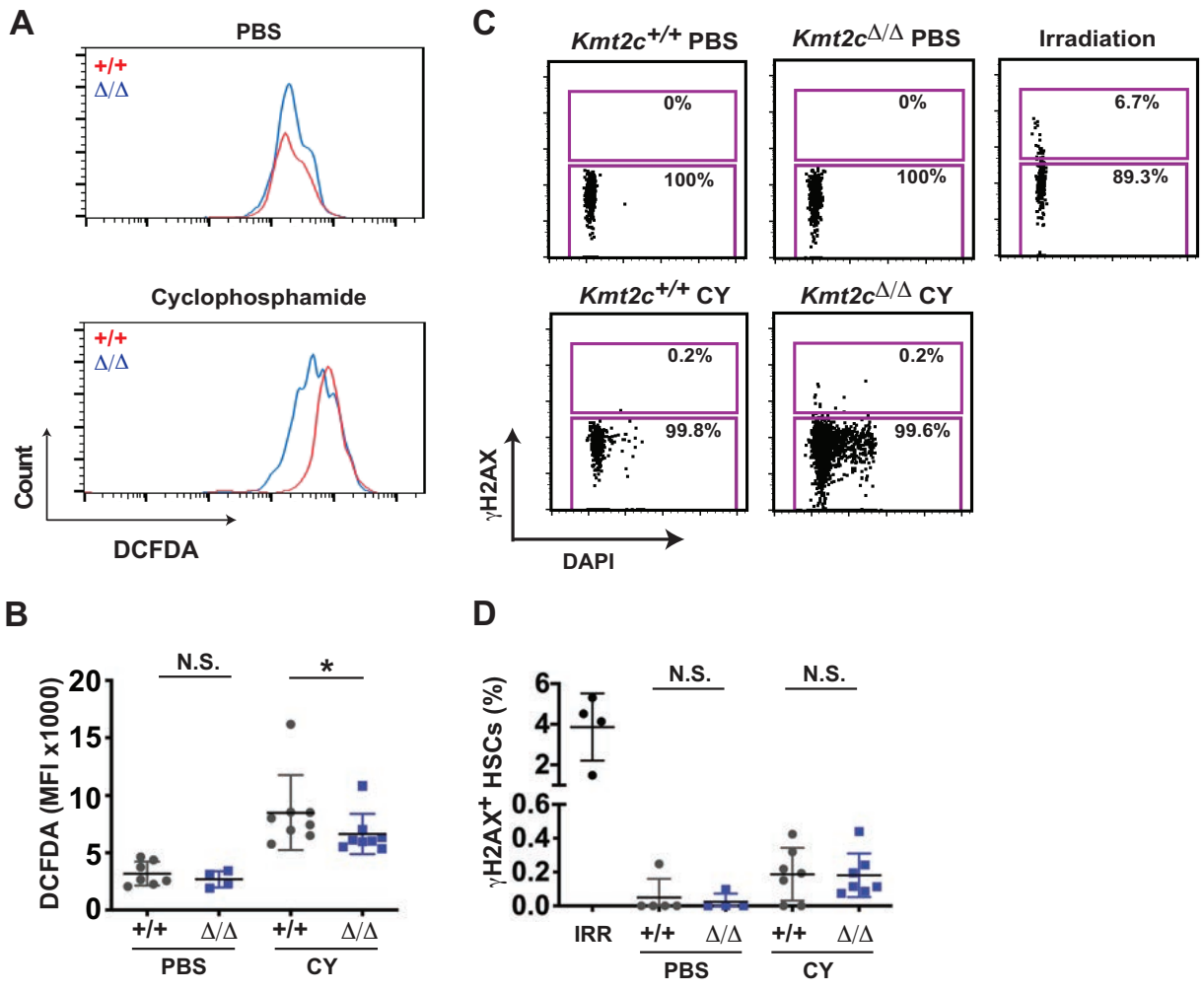

Figure S4 (related to Figure 4). *Kmt2c* deletion has limited effects on ROS levels and DNA damage. (A) Representative histograms showing DCFDA fluorescence in wild type and *Kmt2c*$^{\Delta/\Delta}$ HSCs after vehicle (PBS) or cyclophosphamide treatment. (B) Mean DCFDA fluorescence in wild type and *Kmt2c*$^{\Delta/\Delta}$ HSCs two days after vehicle (PBS) or CY treatment. n=4-8. (C) Representative flow cytometry plots and gating strategy for γH2AX detection in wild type and *Kmt2c*$^{\Delta/\Delta}$ HSCs. Irradiation (600 cGy) was used as a positive control. (D) Percent of wild type and *Kmt2c*$^{\Delta/\Delta}$ HSCs with γH2AX after irradiation (Irr), or 2 days after PBS or CY treatment. n=4-7. Error bars reflect standard deviations. *p<0.05 by two-tailed Student's t-test.

Figure S5

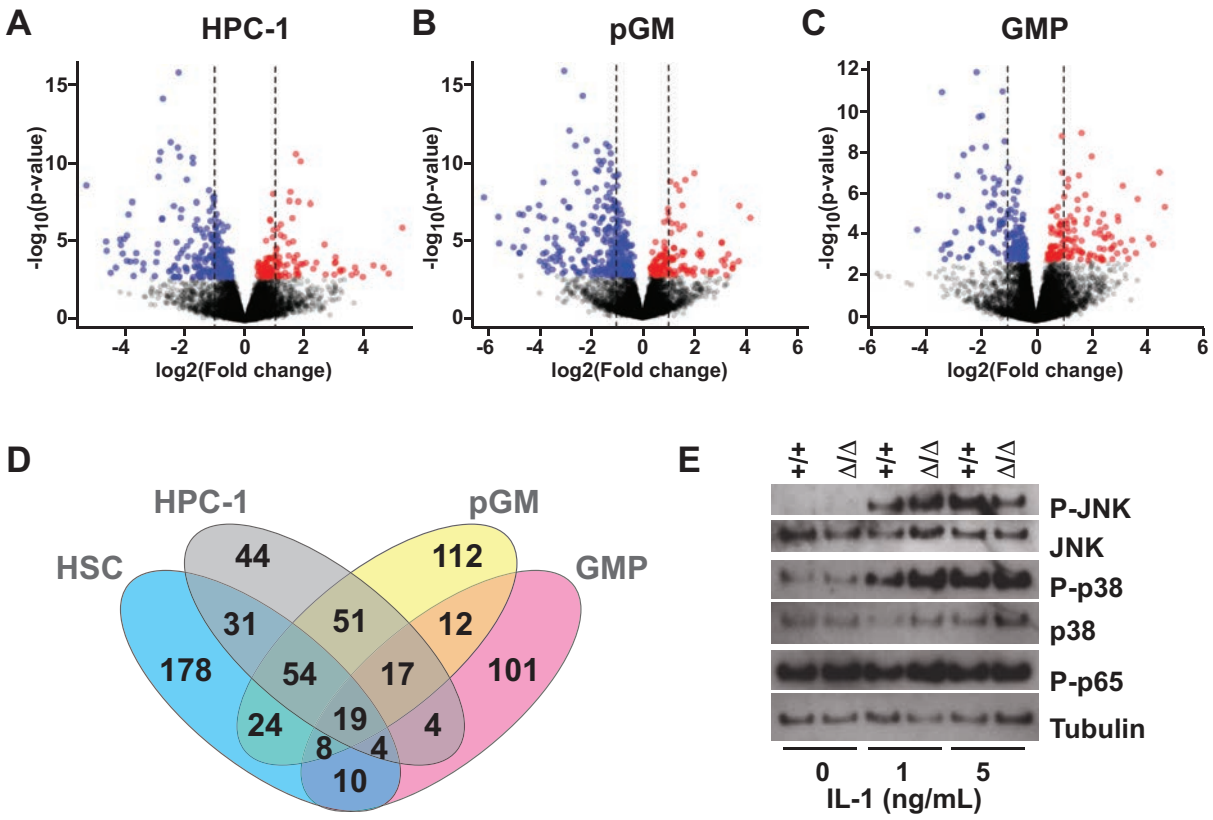

Figure S5 (related to Figure 4). *Kmt2c* deletion blunts IL-1β-driven signal transduction and gene expression changes. (A-C) Volcano plots showing gene expression changes in *Kmt2c*$^{\Delta/\Delta}$ HPC-1, pGM and GMP. n=4 per genotype. Red and blue denote significantly increased or decreased expression after *Kmt2c* deletion (FDR<0.05). n=4. (D) Venn diagram showing the degree of overlap in differentially expressed genes identified by comparing wild type to *Kmt2c*$^{\Delta/\Delta}$ HSCs, HPC-1s, pGMs and GMPs. (E) Western blots showing JNK, p38 and p65 phosphorylation in HPCs after *ex vivo* IL-1β exposure.

Figure S6

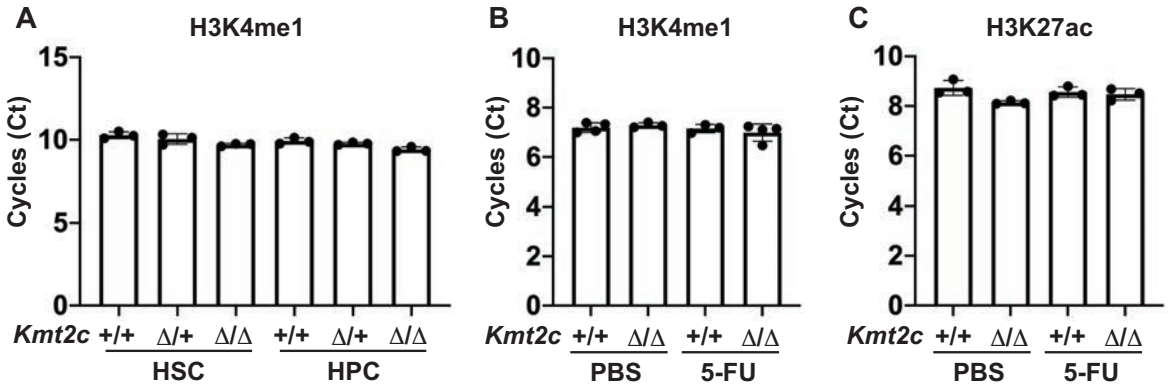

Figure S6 (related to Figures 6 and 7). *Kmt2c* deletion does not alter global H3K4me1 or H3LK27ac levels. (A, B) ChIP-qPCR with tagmented chromatin fragments from 30,000 HSCs after immunoprecipitation with H3K4me1 antibody. Cell types, treatment groups and genotypes are indicated on the x-axis. The ChIP-qPCR shows very little variation in signal among the genotypes and treatment groups, indicating that H3K4me1 levels are not globally depleted in the absence of MLL3. (C) ChIP-qPCR with tagmented chromatin fragments from 50,000 HSCs after immunoprecipitation with H3K4me1 antibody. n=3-4.

Figure S7

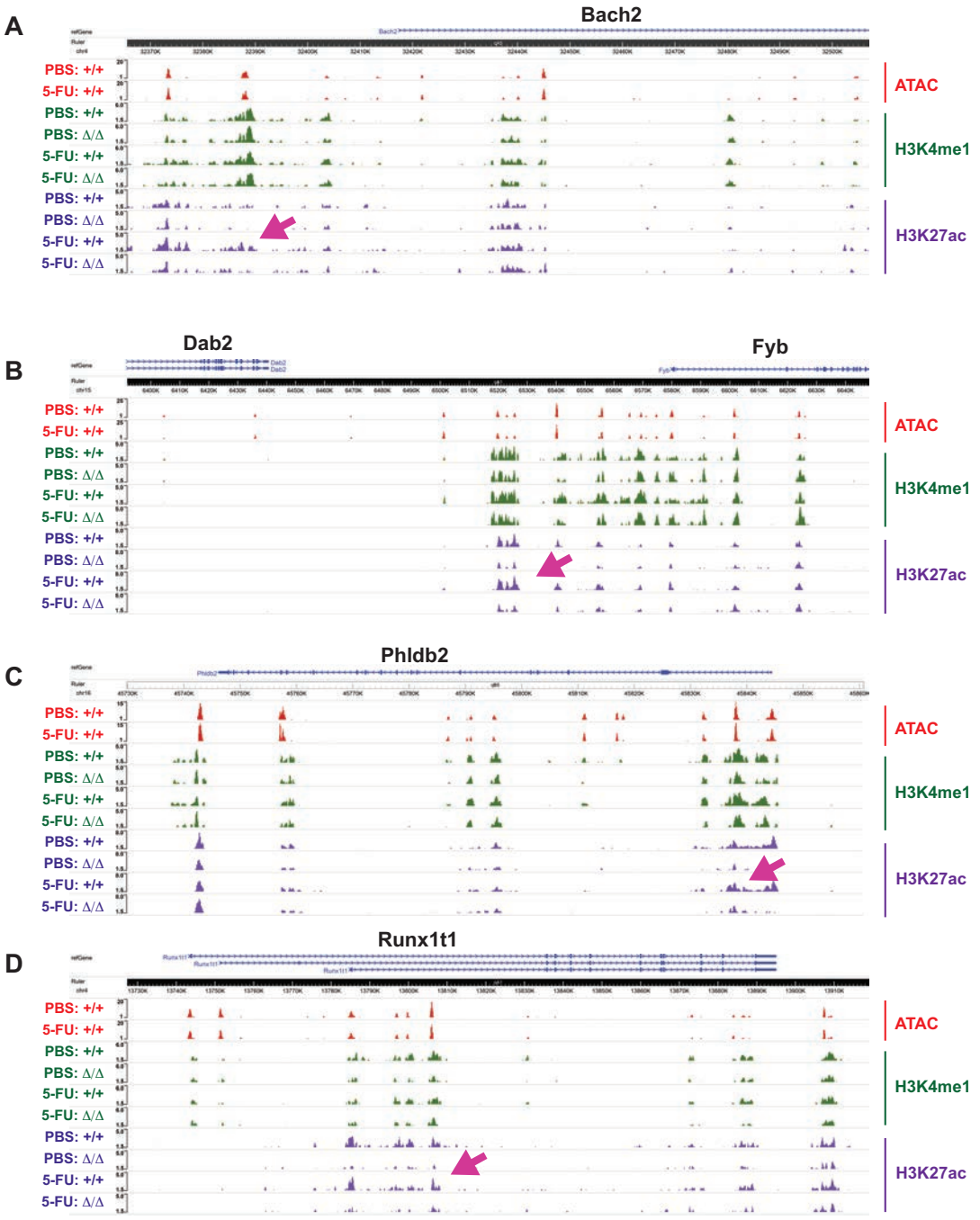

Figure S7 (related to Figure 7). MLL3 promotes enhancer activation after 5-FU treatment. (A-D) Tracks for ATAC-seq, H3K4me1 and H3K27ac levels at five MLL3 target genes – *Bach2* (A), *Dab2* and *Fyb* (B), *Phldb2* (C) and *Runx1t1* (D) – in HSCs after 3 cycles of PBS or 5-FU treatment.